ISSN : 2830-8085
DOI : https://doi.org/10.58452/jpcr.v1i2

Journal of
Physical & Chemical Research

Volume **1,** Issue 2, December (2022) 1-35

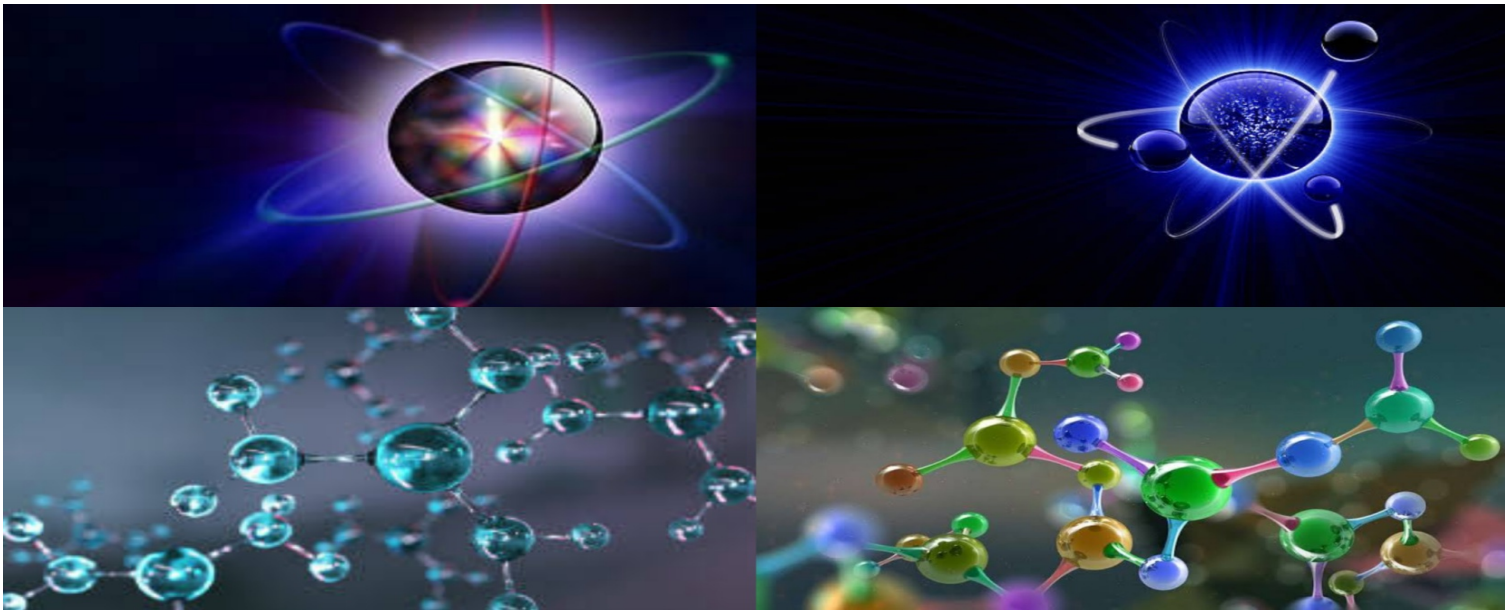

Pr. Kahoul Abdelhalim
Editor-in-Chief

First Legal Deposit: June, 2022

Journal homepage: https://ojs.univ-bba.dz

Journal of Physical and Chemical Research

- **Scientific committee**

- Laraoui Abdelghani
  alaraoui2@unl.edu
  Department of Mechanical & Materials Engineering, University of Nebraska – Lincoln, USA.
- Nuray Kup Aylikci
  nuray.aylikci@iste.edu.tr
  Department of Energy Systems Engineering, Faculty of Engineering and Natural Sciences.
  Iskenderun Technical University, Iskenderun, Hatay, Turkey.
- Volkan Aylikci
  volkan.aylikci@iste.edu.tr
  Department of Metallurgical and Materials Engineering,
  Faculty of Engineering and Natural Sciences, Iskenderun Technical University,
  Iskenderun, Hatay, Turkey.
- Sarra Mustapha
  sarramust1@yahoo.fr
  Mohamed El Bachir El Ibrahimi University, Bordj-Bou-Arreridj, Algeria.
- Latrache Abdelhakim
  abdelhakim.latreche@univ-bba.dz
  Mohamed El Bachir El Ibrahimi University, Bordj-Bou-Arreridj, Algeria.
- Abdelhalim Bencheikh
  abdelhalim.bencheikh@univ-bba.dz
  Mohamed El Bachir El Ibrahimi University, Bordj-Bou-Arreridj, Algeria.
- Bentabet Abdelouahab
  abdelouahab.bentabet@univ-bba.dz
  Mohamed El Bachir El Ibrahimi University, Bordj-Bou-Arreridj, Algeria
- Lebgaa Nodjoud
  noudjoud.lebga@univ-bba.dz
  Mohamed El Bachir El Ibrahimi University, Bordj-Bou-Arreridj, Algeria.
- Bahloul Ahmed
  ahmed.bahloul@univ-bba.dz
  Mohamed El Bachir El Ibrahimi University, Bordj-Bou-Arreridj, Algeria.
- Hellati Abdelhak
  abdelhak.hellati@univ-bba.dz
  Mohamed El Bachir El Ibrahimi University, Bordj-Bou-Arreridj, Algeria.
- Boufassa Samia
  samia.boufassa@univ-bba.dz
  Mohamed El Bachir El Ibrahimi University, Bordj-Bou-Arreridj, Algeria.
- Benamrani Ammar
  ammar.benamrani@univ-bba.dz
  Mohamed El Bachir El Ibrahimi University, Bordj-Bou-Arreridj, Algeria.
- Daoud Salah
  salah.daoud@univ-bba.dz
  Mohamed El Bachir El Ibrahimi University, Bordj-Bou-Arreridj, Algeria.
- Riad Ayache
  riad.ayache@univ-bba.dz
  Mohamed El Bachir El Ibrahimi University, Bordj-Bou-Arreridj, Algeria.
- Khelladi Mohamed Ridha
  mohamedridha.khelladi@univ-bba.dz ; redha2022@yahoo.fr
  Mohamed El Bachir El Ibrahimi University, Bordj-Bou-Arreridj, Algeria.
- Tabti Salima
  salima.tabti@univ-bba.dz ; thabti_sa@yahoo.fr
  Mohamed El Bachir El Ibrahimi University, Bordj-Bou-Arreridj, Algeria.
- Chikouche Imene
  imene.chikouche@univ-bba.dz ; chikouche_imene@yahoo.fr
  Mohamed El Bachir El Ibrahimi University, Bordj-Bou-Arreridj, Algeria.
- Khalfallah Farid
  f.khalfallah@univ-bba.dz ; khal.far@gmail.com
  Mohamed El Bachir El Ibrahimi University, Bordj-Bou-Arreridj, Algeria.
- Daoudi Salim
  s.daoudi@univ-bba.dz ; salzdg@gmail.com
  Mohamed El Bachir El Ibrahimi University, Bordj-Bou-Arreridj, Algeria.

- Sahnoune Yassine
  yassine.sahnoune@univ-bba.dz ; sahnoun.y34@gmail.com
  Mohamed El Bachir El Ibrahimi University, Bordj-Bou-Arreridj, Algeria.
- Bioud Nadhira
  nadhira.bioud@univ-bba.dz
  Mohamed El Bachir El Ibrahimi University, Bordj-Bou-Arreridj, Algeria
- Kasri Yazid
  yazidkasri@yahoo.fr
  University of Béjaia.
- Deghfel Bahri
  badeghfel@gmail.com
  University of M'sila
- Baadji Nadjib
  nadjibbaadji@gmail.com
  University of M'sila
- Lamiri Leila
  l.lamiri@crti.dz
  Unité de Développement des Couches, Minces et Applications (UDCMA-CRTI), Sétif.
- Laidoudi Samiha
  s.laidoudi@crti.dz
  Unité de Développement des Couches, Minces et Applications (UDCMA-CRTI), Sétif.
- Belgherbi Ouafia
  o.belgherbi@crti.dz
  Unité de Développement des Couches, Minces et Applications (UDCMA-CRTI), Sétif.
- Kaabi Ilhem
  Kaabi.ilhem@univ-setif.dz
  Ferhat Abbas University -Sétif 1-, Algeria.
- Boudour Samah
  s.boudour@crti.dz
  Unité de Développement des Couches Minces et Applications (UDCMA-CRTI)
- Belhadj Hamza
  email: hbelhadj@cdta.dz , belhadjhamza@gmail.com
  Unité de Recherche en Nanosciences et Nanotechnologies
  Centre de Développement des Technologies Avancées (CDTA)
- Hamza Djamel
  Email : djamel.hamza@univ-setif.dz
  Département de chimie, Faculté des Sciences, Université Ferhat ABBAS- Sétif 1
- Hayette Faid
  hayettefaid@univ-bba.dz
  Mohamed El Bachir El Ibrahimi University, Bordj-Bou-Arreridj, Algeria.
- Fares Nor El Houda
  norelhouda.fares@univ-bba.dz; fares_houda@yahoo.fr
  Département Recherche Opérationnelle, Faculté Mathématiques et Informatiques Mohamed El Bachir El Ibrahimi University, Bordj-Bou-Arreridj, Algeria

Journal of Physical and Chemical Research
Volume 1 December (2022) 1-35

Physical Research

Journal of Physical & Chemical Research

Journal homepage: https://ojs.univ-bba.dz

Angular and energy dispersion in neutron-rich nuclei by neutron evaporation: A Monte Carlo simulation

Khalfallah Farid[1,2*], **Chia Leila**[1]

[1] *Department of matter science, Faculty of sciences and technology, University of Mohamed El Bachir El Ibrahimi, Bordj Bou Arreridj, 34030 Algeria*
[2]*Laboratory of Materials Physics, Radiation and Nanostructures (LPMRN), Faculty of Sciences and Technology, Mohamed El Bachir El Ibrahimi University, Bordj-Bou-Arreridj 34030, Algeria.*

* *E-mail address: f.khalfallah@univ-bba.dz*
DOI: https://doi.org/10.58452/jpcr.v1i2.20

Article history
Received March 20, 2022
Accepted for publication June 02, 2022

Abstract

In this paper we present the results of a Monte Carlo simulation of the effects of neutron evaporation on the angular and energy dispersions in neutron-rich nuclei as a function of the mass number *A*, the kinetic energy *E* and the number of emitted neutrons. We based our simulation on the assumption of an isotropic random distribution for the neutron emission angles in space and on a Maxwell-Boltzmann distribution for the kinetic energy of the evaporated neutrons. Our results confirm large angular and energy dispersions for light, low-energy nuclei and for high neutron channels.

Keywords: Energy and angular dispersion, fusion reaction, neutron evaporation, neutron rich nuclei, Monte Carlo.

1. Introduction

The emission or evaporation of neutrons in unstable neutron-rich nuclei following fusion-evaporation reactions is a common phenomenon in nuclear reaction physics. This process allows the compound nucleus to lose a significant portion of its excitation energy by evaporating its excess of neutrons during its flight toward the detector. These neutron emissions can have significant effects on the trajectory and kinetic energy of the emitting nucleus and thus affecting the detection efficiency in nuclear detection systems like magnetic separators [1-3]. It can also affect the precision measurements of the implantation energy for focal plane detectors [4].

In this work, we perform a Monte Carlo calculation of the angular and energy effects of neutron evaporation on the residual nucleus. In the field of fusion-evaporation and fission reactions, several Monte Carlo simulations for statistical neutron evaporation and fission fragments has been made notably by Vanderbosh & all [5] and Kawano & al. [6-7]. Recently the field has gained a great interest because of its importance in the fusion of heavy and super-heavy elements [8]. Our calculations consist of a systematic study of neutron's angular and energy dispersion depending on two parameters, the masse number *A* of the nucleus (from relatively light to heavy nuclei) and the neutron emission channel (from *1n* to *5n*). The simulations were carried out using CERN Fortran libraries specialized in the generation of random numbers.

2. Method

The emission of each neutron from the nucleus contributes to the deviation of the trajectory of the evaporation residue as well as to the dispersion of its kinetic energy. Due to the conservation of momentum, one can expect maximum angular deviation of the nucleus when the neutron is emitted in a direction perpendicular to the axis of motion, while if it is emitted in a parallel direction, the deflection will be minimal. For the kinetic energy of the emitting nucleus, It is the opposite that is expected. Parallel neutron emissions contribute to a maximum variation of the energy of the nucleus resulting in a decreasing kinetic energy for a forward emission and an increasing energy for a backward emission. A minimal energy variation occurs if the neutrons are emitted perpendicularly.

In order to evaluate the importance of these two phenomena we perform our Monte Carlo simulation based on two assumptions: First, we suppose an isotropic random distribution of neutron emission angles in space. Second, we consider that each neutron is emitted with a kinetic energy distributed according to a statistical evaporation model of Maxwell-Boltzmann type.

2.1 Angular and energy dispersion

To calculate the deflection angle $\boldsymbol{\theta}$ of the residual nucleus and its kinetic energy $\boldsymbol{E}$ after the emission of several neutrons, we start by writing the kinematic equations representing the movement of the nucleus before and after the emission of a first neutron. Suppose that we have a neutron-rich nucleus Y (figure 1) in an excited state with mass $\boldsymbol{M_Y}$, excitation energy $\boldsymbol{E^*}$, momentum $\boldsymbol{P(Y)}$ and a kinetic energy $\boldsymbol{T_Y}$. The evaporation of the first neutron with kinetic energy $\boldsymbol{T_n}$ occurs through the reaction:

$$ {}^{A}_{Z}Y_N \rightarrow {}^{A-1}_{Z}Y'_{N-1} + 1n \tag{1} $$

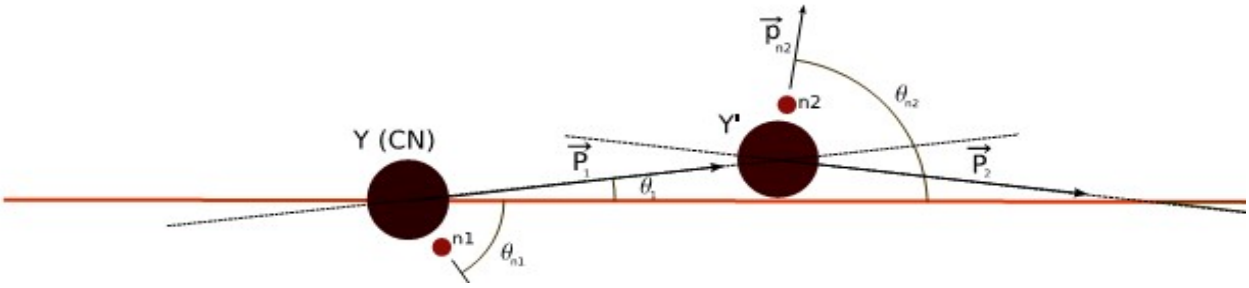

Figure 1. Schematization of the angular deviations of the residual nucleus after the emission of two neutrons.

Conservation of energy and momentum allow us to calculate the energy and momentum of the residual nucleus and of the evaporated neutron.

2.1.1 Conservation of energy and momentum

The application of the principles of momentum and energy conservation on the reaction (1) leads to the following equations for the excitation energy and momentum of the nucleus before and after emission of the first neutron (channel 1n):

$$ \vec{P}(Y) = \vec{P}(Y') + \overrightarrow{P_n} \tag{2} $$

$$E'^{*} = E^{*} - (T_{Y'} - T_Y) - (T_n + S_n) \tag{3}$$

Where

$$S_n = (M_{Y'} - M_Y + M_n)c^2 \tag{4}$$

is the bending energy of the neutron. The kinetic energy $\boldsymbol{T_n}$ of the emitted neutron will be derived from a Maxwell-Boltzmann distribution.

2.1.2 Energy distribution of evaporated neutrons

For our calculation, the energy profile used for the evaporated neutrons is a well known model in statistical physics and neutron physics. It is the model of a neutron gas according to a Maxwell-Boltzmann statistics. In this model, the energy distribution function of the evaporated neutrons is given by a Maxwell-Boltzmann function:

$$f(T_n) = \frac{\sqrt{T_n}}{T^2} e^{-\frac{T_n}{kT}} \tag{5}$$

Where:

$$\boldsymbol{kT \sim \frac{E^{*}}{\sqrt{A/8}}}$$

is the temperature of the nucleus which is proportional to its excitation energy.

2.1.3 Recurrence relations for angular deviation and energy

For the subsequent neutron emissions (2n, 3n... 5n channels), using the same principles at every step of a second neutron evaporation we can derive the following recurrence relations between the excitation energy of the residue, its momentum and the neutron energy before and after the emission of the k-*th* neutron.

$$\overrightarrow{P_{k+1}} = \overrightarrow{P_k} - \overrightarrow{P_{n,k}} \tag{6}$$

$$E^{*}_{k+1} = E^{*}_k + (T_k - T_{k+1}) - (T_n + S_{nk} \tag{7}$$

$$S_{nk} = (My_{k+1} + M_n - M_{Y_k})c^2 \tag{8}$$

In spherical coordinates, where the z axis is the direction of the movement of the nucleus, if $\boldsymbol{\theta_k}$ and $\boldsymbol{\varphi_k}$, $\boldsymbol{\varphi_{k+1}}$ and $\boldsymbol{\theta_{k+1}}$ are the angular coordinates of the nucleus before and after emission of the k-*th* neutron then we have:

$$\begin{cases} P_{k+1}\sin\theta_{k+1}\cos\varphi_{k+1} = P_k\sin\theta_k\cos\varphi_k - p_{nk}\sin\theta_{nk}\cos\varphi_{nk} = f_{xk} \\ P_{k+1}\sin\theta_{k+1}\sin\varphi_{k+1} = P_k\sin\theta_k\sin\varphi_k - p_{nk}\sin\theta_{nk}\sin\varphi_{nk} = f_{yk} \\ P_{k+1}\cos\theta_{k+1} = P_k\cos\theta_k - p_{nk}\cos\theta_{nk} = f_{zk} \end{cases} \tag{9}$$

The right hand side of these equations are functions of the angular and momentum variables at the *k*-step and are labelled: $\boldsymbol{f_{xk}}$, $\boldsymbol{f_{yk}}$, $\boldsymbol{f_{zk}}$.

Using these functions we finally obtain the energies and angular variables of the evaporation residue at the (*k+1*)-step :

$$\begin{cases} T_{k+1} = \frac{P_{k+1}^2}{2M_{Y_{k+1}}} = \frac{f_{xk}^2+f_{yk}^2+f_{zk}^2}{2M_{Y_{k+1}}} \\ cos\theta_{k+1} = \frac{f_{zk}}{\sqrt{f_{xk}^2+f_{yk}^2+f_{zk}^2}} \\ \cos\varphi_{k+1} = \frac{f_{xk}}{\sqrt{f_{xk}^2+f_{yk}^2}} \end{cases} \quad (10)$$

2.2 Monte-Carlo simulation

The Monte Carlo method [9-10] is used in our simulation, it is a stochastic method that allow us to introduce the randomness inherent to this type of nuclear interactions. The calculation of the energies and angles at each neutron emission is performed from the recurrence relations (9) and (10), the angle of deviation of the evaporation residues θ_{k+1} represents the deviation of the nuclei with respect to the initial axis of trajectory after evaporation of k neutrons.

The emission of neutrons can occur randomly in any direction in space, to obtain an isotropic distribution of the direction of emission, we use a uniform random numbers generator. Therefore, at each iteration, the azimuth angle φ_{nk} is generated uniformly between 0 and 2π and the cosine of the angle θ_{nk} is generated uniformly between -1 and 1. The neutrons momenta are deduced from their energies. As mentioned above, the statistical evaporation of neutrons follows a Maxwell-Boltzmann distribution, thus the neutron energies are generated according to this distribution. The random number generators used in our calculations are part of the CERN Fortran library.

3. Results

The Monte-Carlo simulation was performed for a wide range of the mass A of the nuclei from A= 40 (light nuclei) to A=260 (heavy nuclei) with a 20-units step.

For each value of A, we simulated a number of 20000 nuclei and for each nucleus the five channels 1n, 2n, 3n, 4n and 5n (cold and hot fusion) where considered. All the calculations were made for 2 values of the initial kinetic energy of the emitting nucleus: E=10MeV and E=50MeV. For the initial excitation energies E* of the nuclei, we worked with two values, E*=30MeV for the nuclei with initial kinetic energy E=10MeV and E*=60MeV for the more the energetic nuclei with initial energy of 50 MeV.

The result of the simulation is presented in the figures below plotted in the form of histograms for light (A=40, 60, 80) and heavy (A=220, 240, 260) nuclei. The angular and energy distribution of the evaporation residue are shown for the 3n channel only with a polynomial fit for the angular part and a Gaussian fit for the energy part (red lines). Similar distributions were obtained for the other 1n, 2n, 4n and 5n channels.

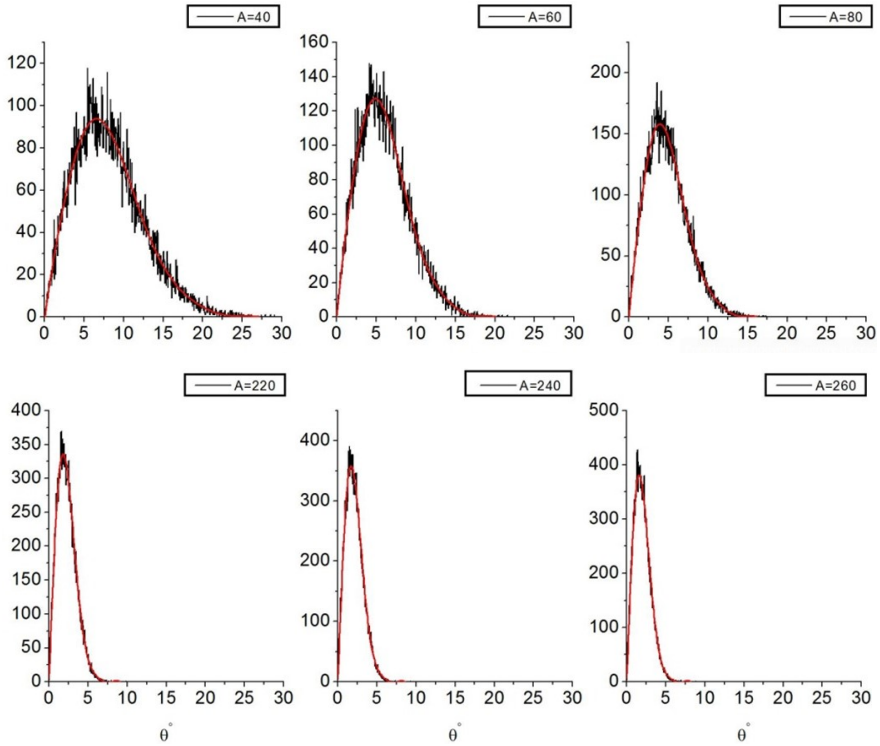

Figure 2. Angular distribution of the evaporation residue for E=10MeV - 3n channel

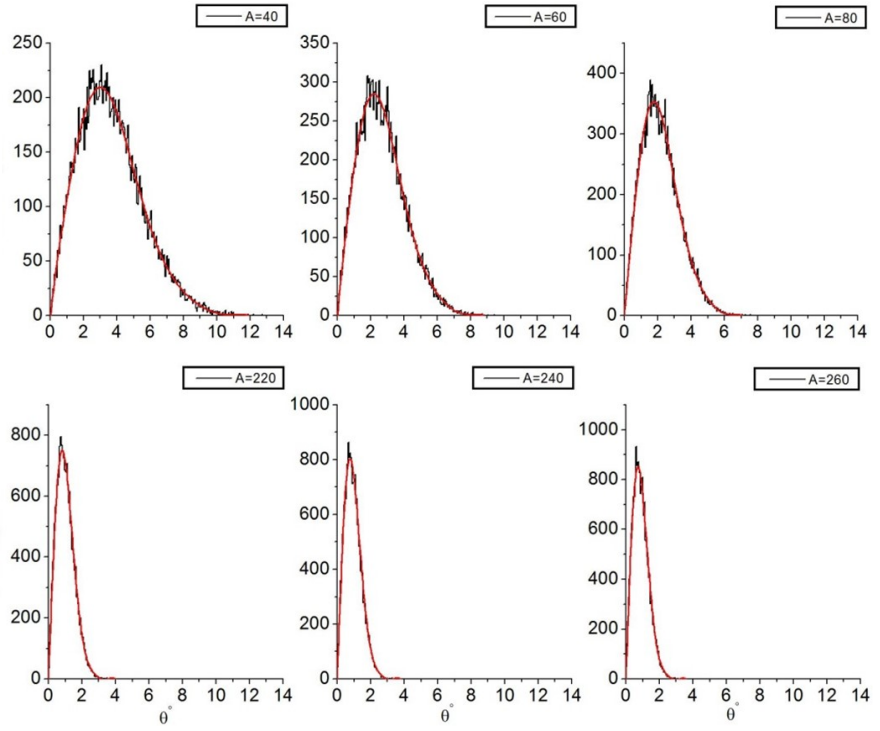

Figure 3. Angular distribution of the evaporation residue for E=50MeV - 3n channel

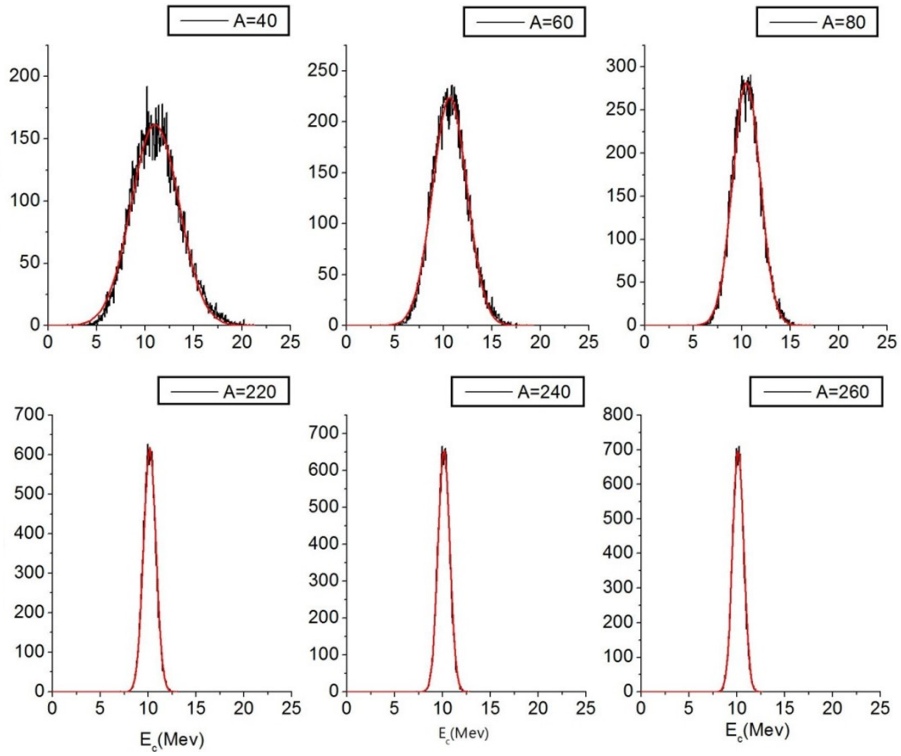

Figure 4. Energy distribution of the evaporation residue for E=10MeV - 3n channel

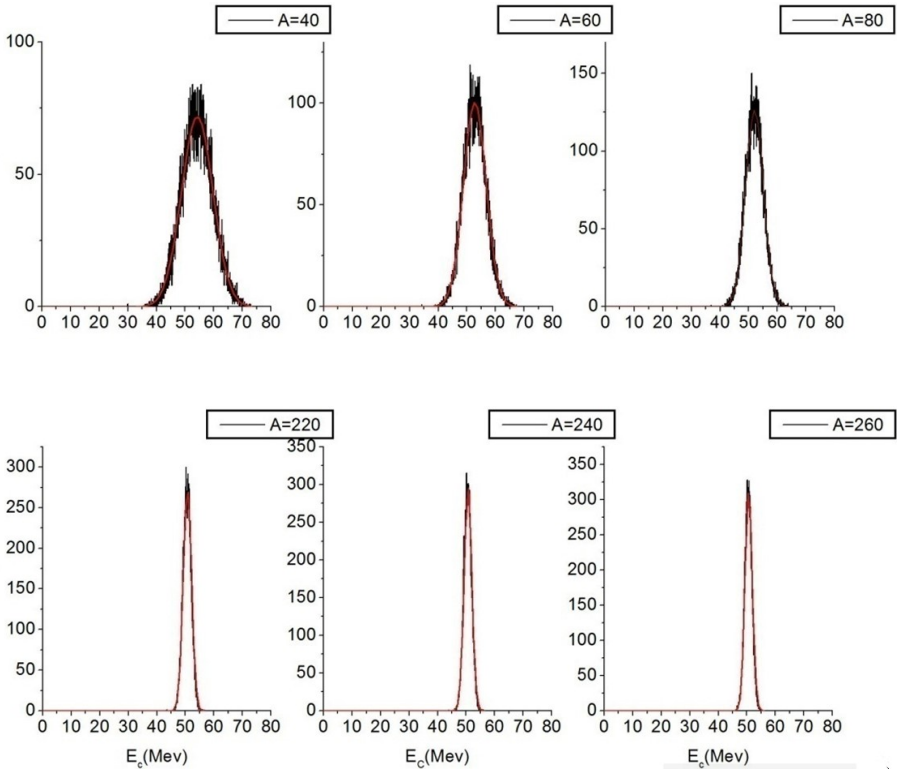

Figure 5. Energy distribution of the evaporation residue for E=50MeV - 3n channel

From the figures of the angular distributions (figures 2 & 3) we clearly see that the vast majority of the residue (after 3 neutrons evaporation) are concentrated in a region around a maximum angle θ_{max}. We observed the same behaviour for the other channels. The nuclei are concentrated in a crown around the axis of movement and the central region corresponding to the axis of motion (θ=0) is almost empty of nuclei. We also observe that the distributions are wider for light nuclei and become narrower with increasing mass number A.

For the energy spectra (figures 4 & 5), we observe normal (Gaussian) distributions with a decreasing widths FWHM (Full Weight Half Maximum). The widths are larger for light nuclei and decrease with increasing nucleus mass. One also notices a light shift of the average value of the energy (the center of the normal curve) compared to its initial values.

In order to examine more closely the influence of the number of neutrons emitted as a function of the mass of the nuclei A and make a comparison between the two cases of low (E=10MeV) and high (E=50Mev) initial energy we extracted the maximum values of the angular dispersion θ_{max} (the dominant angle of deviation). On the other hand, to evaluate the importance of the energy dispersion, we also extracted the widths of the energy spectra FWHM.

These values are shown in the following tables and the corresponding plots are presented below.

Table 1. Dominant angular dispersion θ_{max} (in degree) for E=10MeV

Channel	A=60	A=100	A=140	A=180	A=220	A=260
1n	2.318	1.550	1.203	1.010	0.875	0.754
2n	3.302	2.303	1.819	1.499	1.298	1.146
3n	4.921	3.299	2.585	2.156	1.806	1.594
4n	5.778	3.951	2.961	2.442	2.110	1.892
5n	6.128	4.413	3.399	2.815	2.427	2.128

Table 2. Dominant angular dispersion θ_{max} (in degree) for E=50MeV

Channel	A=60	A=100	A=140	A=180	A=220	A=260
1n	1.022	0.694	0.532	0.454	0.380	0.339
2n	1.463	1.017	0.797	0.661	0.571	0.488
3n	2.385	1.498	1.139	0.943	0.839	0.707
4n	2.518	1.760	1.344	1.118	1.000	0.836
5n	2.653	1.897	1.484	1.237	1.071	0.938

Table 3. Energy distribution width FWHM (in MeV) for E=10MeV

Channel	A=60	A=100	A=140	A=180	A=220	A=260
1n	1.652	1.119	0.868	0.718	0.617	0.544
2n	2.392	1.604	1.239	1.024	0.879	0.774
3n	3.552	2.375	1.830	1.509	1.294	1.139
4n	4.186	2.753	2.107	1.741	1.487	1.308
5n	4.649	3.160	2.422	1.978	1.702	1.496

Table 4. Energy distribution width FWHM (in MeV) for E=50MeV

Channel	A=60	A=100	A=140	A=180	A=220	A=260
1n	3.695	2.503	1.938	1.603	1.378	1.215
2n	5.345	3.605	2.776	2.295	1.968	1.736
3n	7.948	5.310	4.089	3.371	2.890	2.545
4n	9.161	6.160	4.717	3.892	3.325	2.926
5n	9.792	7.047	5.373	4.360	3.785	3.310

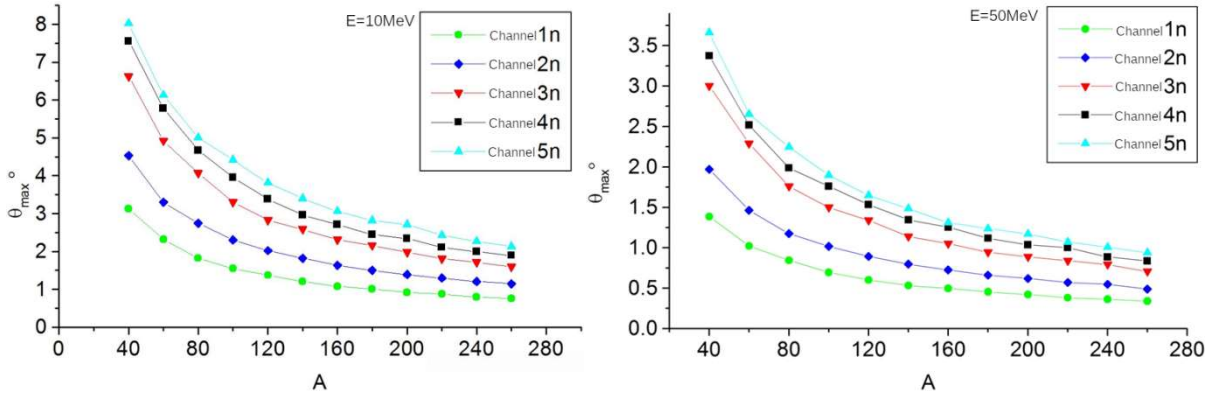

Figure 6. Dominant angular dispersion θ_{max} (all 5 channels) for E=10MeV and E=50MeV

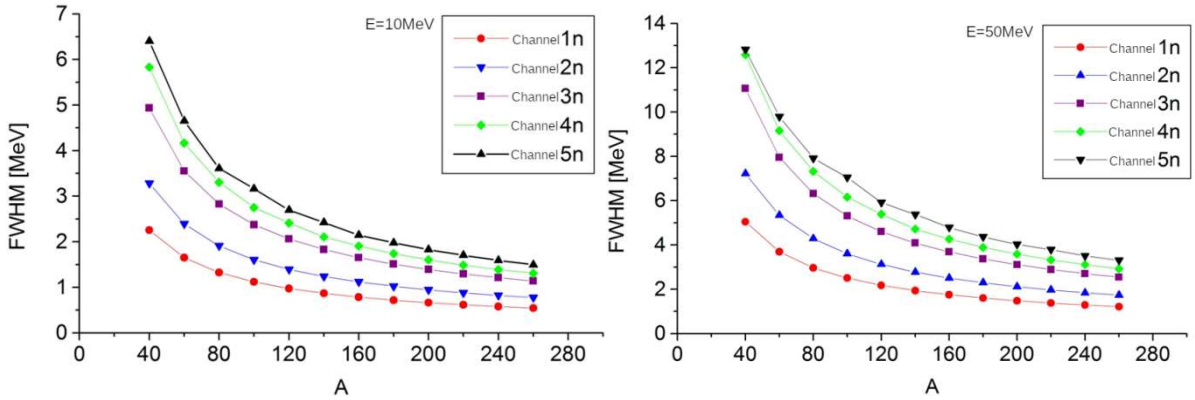

Figure 7. Energy distribution widths FWHM (all 5 channels) for E=10MeV and E=50MeV

4. Discussion

The Monte Carlo simulation shows that the angular dispersion of the residual nuclei, given by θ_{max} (figures 6), has the same decreasing tendency with increasing mass number A for all channels independently of the initial energy of the nucleus.. This observation was predictable since a heavy nucleus has more inertia and momentum (at equal energies) than a light one and is therefore more difficult to deflect by neutron emission. We notice that the decrease is however more pronounced for the high neutron channel. We also observe that θ_{max} increases with the number of neutrons emitted independently of the mass of the nucleus and its initial energy. This increase is more visible for light nuclei. At last, by comparing curves from E=10MeV and E=50MeV, it can be seen that the angular deviations are less important for E=50MeV. This observation was also expected since the more energetic nuclei are more difficult to deflect. These results are in agreement with measurements in experimental detection systems.

For the case of the energy dispersion estimated by the distribution's width FWHM, figures 7 shows a predictable decrease with mass number A for all channels and for the two initial energy values. However, the decreases are greater for multiple neutron emission. We also observe that the widths are wider for E=10MeV (up to 6.4MeV) in comparison with that corresponding to E=50MeV (up to 12.8MeV) independently of the number of neutrons emitted.

5. Conclusion

Our Monte Carlo calculations led to several results, the most important is the fact that the emission of neutrons has the effect of deflecting the majority of the emitting nuclei inside a corona with a wider angle for light and low energy nuclei and for high neutron channels. These deviations can reach up to 8° for the 4n and 5n channels in light nuclei and must be taken into account in the estimation of the efficiency of detection systems. On the other hand, it has been found that the energy dispersion of nuclei is greater for light and low-energy nuclei in the 4n and 5n emission channels, it can reach 3.2MeV for light nuclei having low energies of 10MeV and will therefore have a significant influence on the energy measurements in focal plane detectors.

References

[1] J. Uusitalo & al, Nuclear Instruments and Methods in Physics Research B, v. 204, 638-643 (2003)
[2] I.H. Lazarus & al., IEEE Trans. Nucl. Sci. 48, 567 (2001)
[3] H. Savajols, Nuc. Phys. A 654, 1027 -1032 (1999)
[4] R. D. Page et al, Nuclear Instruments and Methods in Physics Research B, v. 204, 634-637 (2003)
[5] R.Vandenbosch & al., Nuc. Phys. 25 511-521 (1961)
[6] T. Kawano & al., EPJ Web of Conferences 21, 04001 (2012)
[7] T. Kawano & al., Nuc. Phys. A 913, 51-70 (2013)
[8] P. Armbruster, Annual Review of Nuclear and Particle Science 50, 411-479 (2000)
[9] M. H .Kalos, W. A. Paula. Monte Carlo Methods, WILEY-VCH, (2008)
[10] P.R.Cheistian, C.George, Méthodes de Monte Carlo avec R, Springer-Verlag, France (2011).

Journal of Physical & Chemical Research

Journal homepage: https://ojs.univ-bba.dz

Free space dynamics of Laguerre-Gaussian-vortex beam

Assia Yousfi [1*], Abdelhalim Bencheikh [1, 2], Madjeda kherif [1], Abdeljalil Benstiti [1], Saoussane Chabou [1], Ouis Chouaib Boumeddine [1].

[1] *Applied Optics Laboratory, Institute Of Optics And Precision Mechanics, Ferhat Abbas University, Setif 1, Setif 19000, Algeria.*

[2] *Department of Electromechanics, Faculty of Sciences and Technology, University of Bordj Bou Arreridj, BBA 34000, Algeria.*

** Corresponding author: Tel. /Fax: +213792744320; E-mail address: yousfiassia2@gmail.com ; assia.yousfi@univ-setif.dz*

DOI: https://doi.org/10.58452/jpcr.v1i2.22

Article history
Received March 22, 2022
Accepted for publication June 10, 2022

Abstract

In this paper, we analytically demonstrate the propagation of a useful structured light laser beam; namely, the vortex Laguerre-Gaussian beam, the latter is an eigenmode of free space propagation, which is invariant under propagation in lossless systems. Through some numerical simulations, we show the main spatial features of such interesting beams.

Keywords : Optical vortex, vortex Laguerre-Gaussian beams, propagation

1. Introduction

In recent years, research interests have been focused on the study and generation of light beam vortices [1-2]. Vortices are a common phenomenon that is widely found in different physics areas including optics [3-4]. While, an optical vortex is an optical field with zero intensity and an undefined phase value, due to the twisting of the light field around the propagation axis [5]. Such light is characterized by a helical wavefront with a phase singularity [6]. In optics, phase singularity is a phase defect point (in 2D) or a line (in 3D) where the phase is indeterminate and the amplitude equals zero.

The most common optical vortices are vortex Laguerre-Gaussian beams, these latter have concentric rings and a spiral wavefront described by $exp(il\varphi)$, where (l) is a topological charge [7]. Due to their distinct characteristics, these beams have found many applications, in particular; telecommunications [8], spatial multiplexing [9], and optical tweezers [10].

In this work, we discuss the propagation of different vortex Laguerre-Gaussian beams in the longitudinal and transversal planes, showing the intensity and the phase of different obtained shapes for different topological charges.

2. Free-space dynamics of Laguerre Gaussian vortex beam:

The optical filed of Laguerre-Gaussian beam at $z = 0$ in cylindrical coordinates is expressed as:

$$\mathrm{E_{LG}(r_0,\theta,0)=E_0\left(\sqrt{2}\frac{r_0}{w_0}\right)^{|l|}L_p^{|l|}\left(2\frac{r_0^2}{w_0^2}\right)e^{\left(-\frac{{r_0}^2}{w_0^2}\right)}e^{-il}}\quad . \tag{1}$$

Where r_0, θ represent the radial and azimuthal coordinates, respectively. $L_p^{|l|}$ denotes the Laguerre polynomial with p and l indices.
The dynamics propagation of vortex laser beams through ABCD system is governed by the Collins integral given in cylindrical coordinates by [11]

$$\mathrm{E_{out}(r,\varphi,z)=\frac{ik}{2\pi B}.e^{(ikz)}e^{\left(\frac{ikD}{2B}r^2\right)}\int_0^{2\pi}\int_0^{\infty}E_{LG}\,(r_0,\theta,0)Exp\left(\frac{ik}{2B}[A{r_0}^2-2rr_0\cos(\theta-\varphi)]\right)r_0dr_0d\theta} \tag{2}$$

For free space propagation the Matrix elements A=1 and B=z, the Collins integral becomes:

$$\mathrm{E_{out}(r,\varphi,z)=\frac{ik}{2\pi z}.e^{(ikz)}e^{\left(\frac{ik}{2z}r^2\right)}\int_0^{2\pi}\int_0^{\infty}E_{LG}\,(r_0,\theta,0)Exp\left(\frac{ik}{2z}[{r_0}^2-2rr_0\cos(\theta-\varphi)]\right)r_0dr_0d\theta} \tag{3}$$

When we substitute equation (1) into equation (3), we obtain:

$$E_{out}(r,\varphi,z)=\frac{ik}{2\pi z}.e^{(ikz)}e^{\left(\frac{ik}{2z}r^2\right)}\int_0^{2\pi}\int_0^{\infty}E_0\left(\sqrt{2}\frac{r_0}{w_0}\right)^{|l|}L_p^{|l|}\left(2\frac{r_0^2}{w_0^2}\right)e^{\left(-\frac{{r_0}^2}{w_0^2}\right)}e^{-il\theta}\,Exp\left(\frac{ik}{2z}[{r_0}^2-2rr_0\cos(\theta-\varphi)]\right)r_0dr_0d\theta \tag{4}$$

We use the following integral formulas [12]:

$$\int_0^{2\pi}\mathrm{Exp}\left(-\frac{ik}{B}[r_1r_2\cos(\varphi_1-\varphi_2)]\right)\,e^{-il\varphi_1}d\varphi_1=2\pi(-i)^l\exp(-il\varphi_2)J_l\left(\frac{kr_1r_2}{B}\right) \tag{5}$$

With J_l is the Bessel function of order l.
And

$$\int_0^{\infty}x^{l+1}\mathrm{Exp}(-\beta x^2)L_p^l(\alpha x^2)J_1(yx)\,dx=2^{-l-1}\beta^{-l-p-1}\times(\beta-\alpha)^p y^l\mathrm{Exp}\left(-\frac{y^2}{4\beta}\right)L_p^l\left(\frac{\alpha y^2}{4\beta(2-\beta)}\right) \tag{6}$$

After some algebra, the propagation of the LG beam is expressed as:

$$\mathrm{E_{out}(r,\varphi,z)=\frac{ik}{2w_0^2z}.e^{(ikz)}.e^{\left(\frac{ik}{2z}r^2\right)}.\left(-i\frac{\sqrt{2}kr}{2zw_0^2}\right)^{|l|}\left(\frac{1}{w_0^2}-\frac{ik}{2z}\right)^{-l-p-1}}$$
$$\times\exp(-il\varphi)\left(\left(\frac{1}{w_0^2}-\frac{ik}{2z}\right)-2\right)^p\mathrm{Exp}\left(-\frac{k^2r^2}{4z^2\left(\frac{1}{w_0^2}-\frac{ik}{2z}\right)}\right)L_p^{|l|}\left(\frac{k^2r^2}{2z^2\left(\frac{1}{w_0^2}-\frac{ik}{2z}\right)\left(2-\left(\frac{1}{w_0^2}-\frac{ik}{2z}\right)\right)}\right) \tag{7}$$

By multiplying the filed expression by its conjugate, the intensity becomes:

$$I_{out}=\mathrm{E_{out}(r,\varphi,z)}\times E_{out}^*(r,\varphi,z) \tag{8}$$

3. Results:

In this section, in order to investigate the propagation behavior of vortex Laguerre-Gaussian beam, we use equations (7), (8), where we present the intensity distribution of the beam as well as its phase.

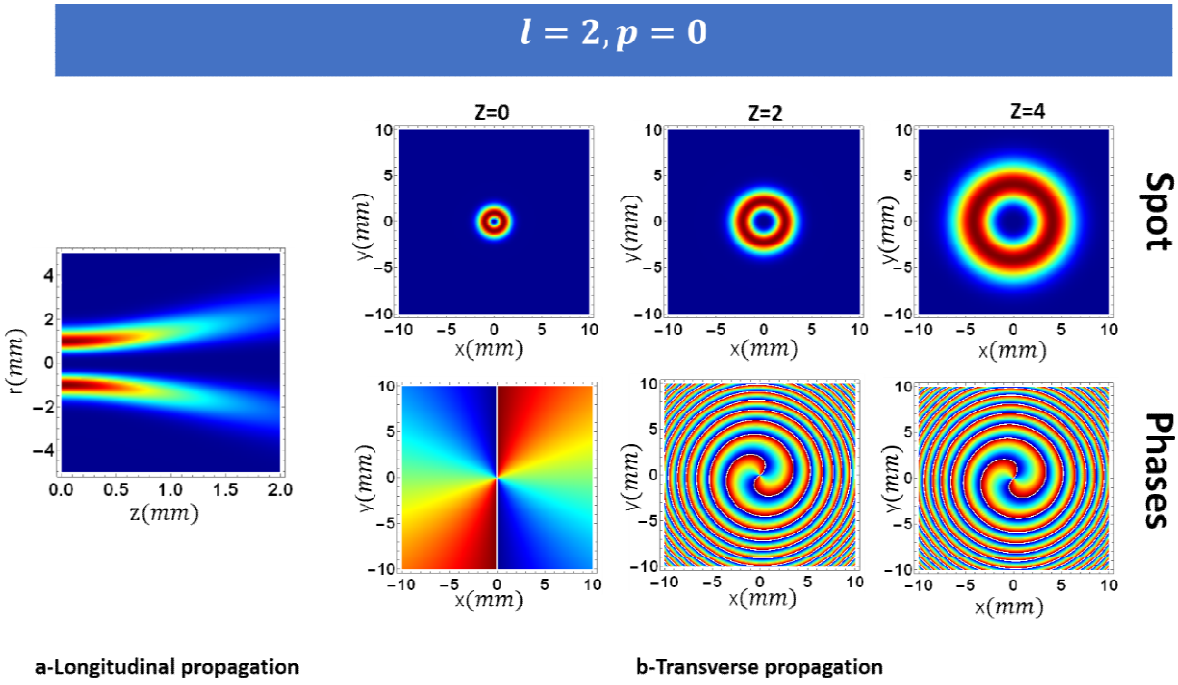

Figure 1: Longitudinal and transverse propagation of LG_0^2 beams representions in both intensity and phase.

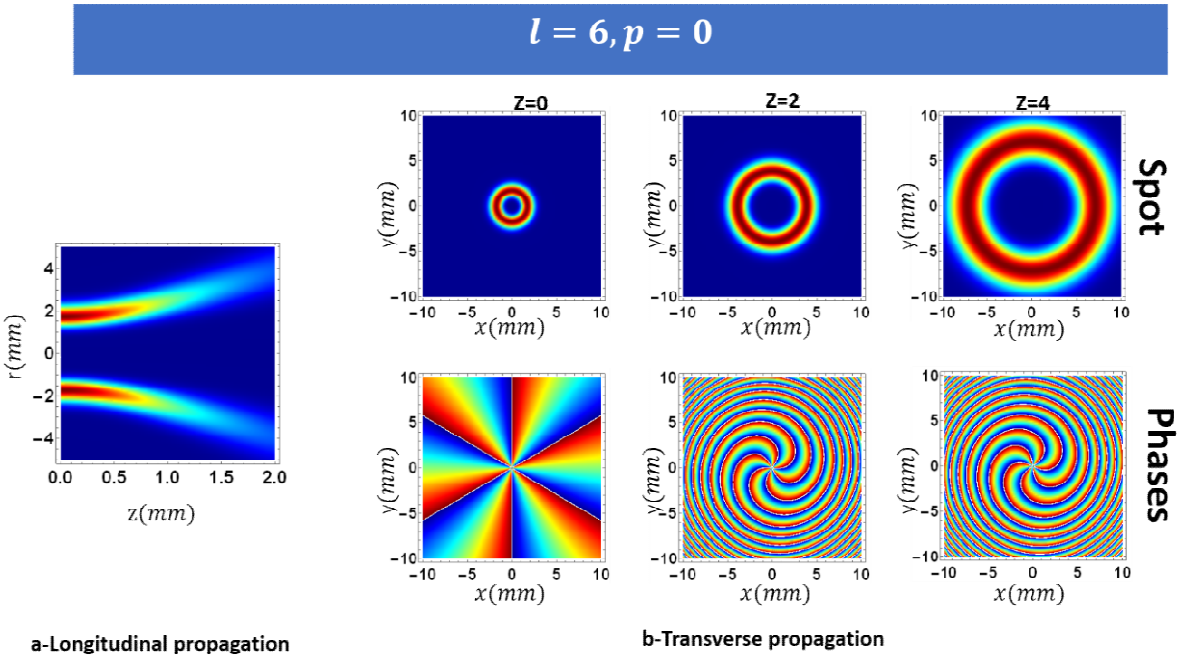

Figure 2: Longitudinal and transverse propagation of LG_0^6 beams representions in both intensity and phase.

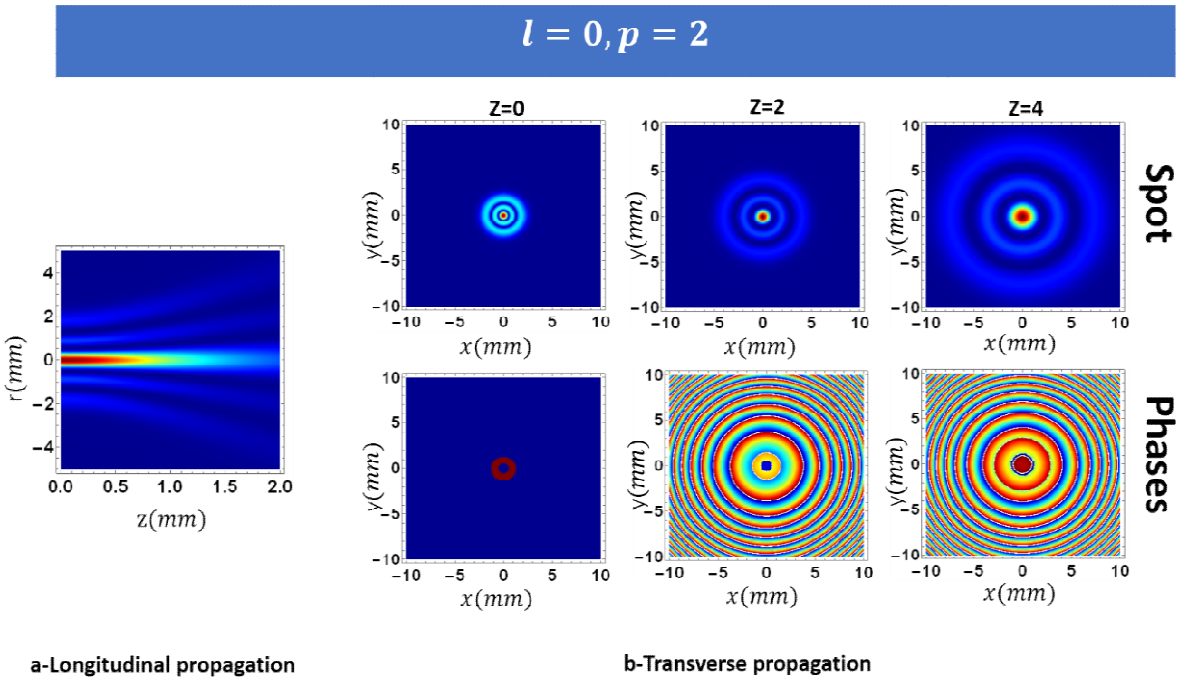

Figure 3: Longitudinal and transverse propagation of LG_2^0 beams representions in both intensity and phase.

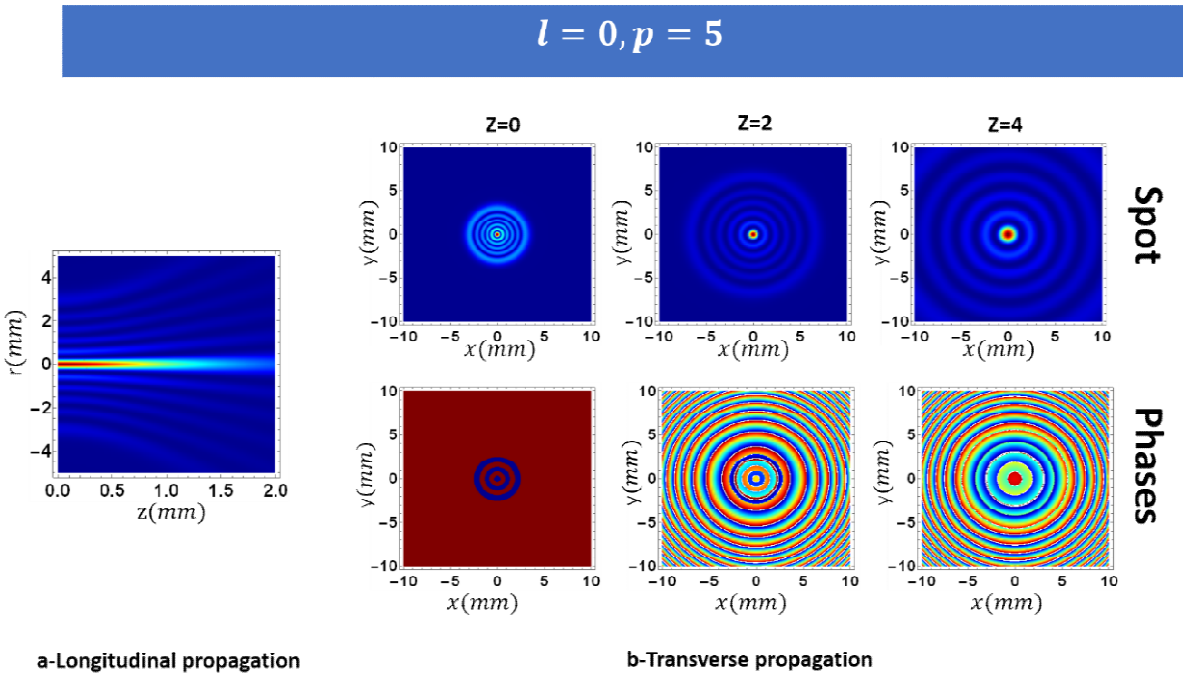

Figure 4: Longitudinal and transverse propagation of LG_5^0 beams representions in both intensity and phase.

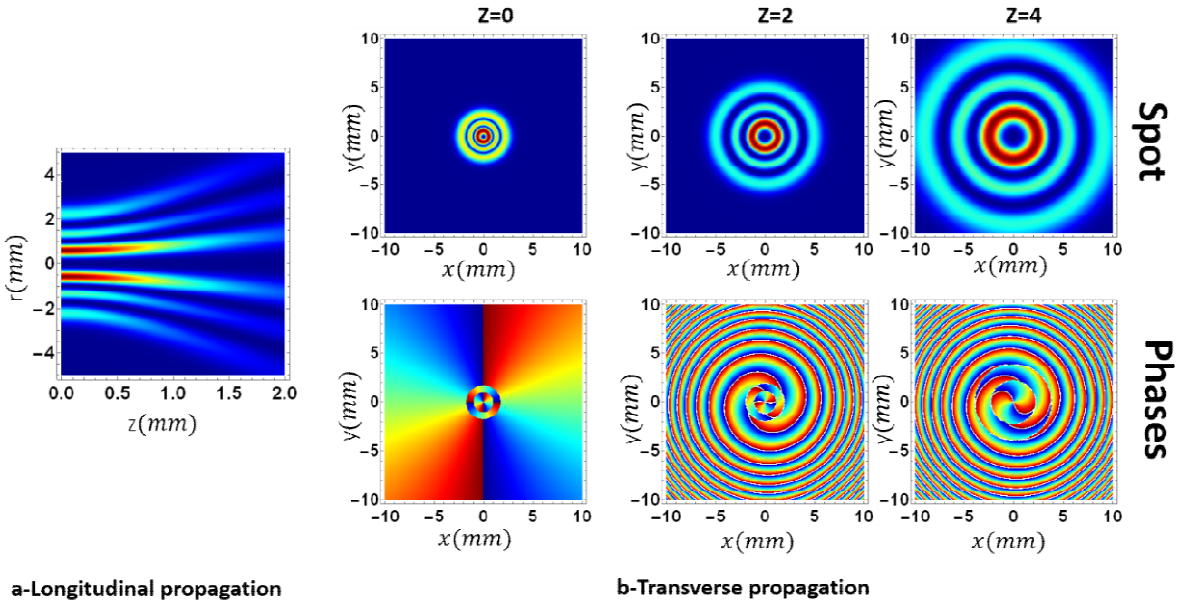

Figure 5: Longitudinal and transverse propagation of LG_2^2 beams representions in both intensity and phase.

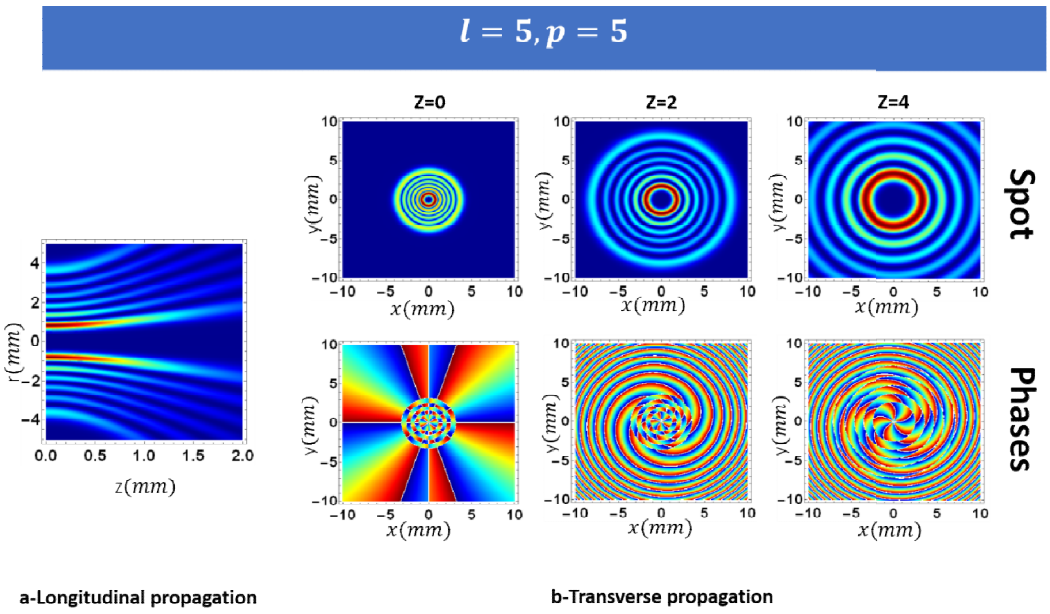

Figure 6: Longitudinal and transverse propagation of LG_5^5 beams representions in both intensity and phase.

4. Discussion:

From the obtained results, the vortex Laguerre-Gaussian beam keeps its shape during the propagation. In figures, (1,2,5,6) the beam has a dark center with large ring, which depends on the beam order. In addition, the phase rotates clockwise during propagation. Meanwhile in figures, (3,4) the vortex Laguerre-Gaussian beam has a bright center surrounded by concentric rings in both intensity and phase profiles. The number of the bright rings depends on the radial order.

5. Conclusion:

In conclusion, we have demonstrated analytically using Collins integral and ABCD matrix, that the Laguerre-Gaussian beam remains vortex Laguerre-Gaussian beam in free space propagation, which means (the beam keeps its structure during propagation)

We have confirmed the obtained results by simulations, such us the invariance structure of the amplitude and phase under free space propagation. Such conclusion, make these beams a good candidate for free space communication, spatial multiplexing and metrology.

References:

[1] N.R. Heckenberg, R. McDuff, C. P. Smith, H. Rubinsztein-Dunlop, M. J. Wegener, *J. Optical and quantum electronics* 24(9) (1992) S951-S962.
[2] S.M. Barnett, L. Allen, *J. Optics communications* 110(5-6) (1994). 670-678.
[3] G. Indebetouw, J. Modern Optics 40(1) (1993) 73-87.
[4] M. R. Dennis, K. O'holleran, M.J. Padgett, *J. Progress in optics-Elsevier* (2009) (Vol. 53, pp. 293-363).
[5] G.F. Brand, J. Physics 67.1 (1999) 55-60.
[6] F. Flossmann, U. T. Schwarz, M. Maier, *J. Optics Communications* 250(4-6) (2005) 218-230
[7] J. Wang, *J. Photonics Research* 4.5 (2016).
[8] J. Wang, *J. Photonics Research* 4(5) (2016) B14-B28.
[9] L. Hadžievski, A. Maluckov, A. M. Rubenchik, S. Turitsyn, *Light: Science & Applications* 4(8) (2015) e314-e314.
[10] D. G. Grier, *J. Nature* 424(6950) (2003) 810-816.
[11] S. A Collins, *JOSA* 60(9) (1970) 1168-1177.
[12] Z. Mei, D. Zhao, *JOSA A* 21(12) (2004) 2375-2381.

J. Phys. & Chem. Res. **1**, Issue 2, December (2022) 16–24

Journal of Physical & Chemical Research

Journal homepage: https://ojs.univ-bba.dz

Theoretical study of second and third order elastic constants of β-SiC

N. Lebga[1,2*], K. Bouamama[2], P. Djemia[3] and S. Mourad Chérif[3]

[1]*Mohamed Elbachir Elibrahimi University, 34000 El-Annaseur, Bordj Bou-Arreridj Algeria*
[2]*Optoelectronics and composant Laboratoiry, Ferhat Abbas University, 19000 Sétif, Algeria*
[3]*LPMTM, UPR CNRS 9001, Paris-Nord University, 93430 Villetaneuse, France*

* Corresponding author: Tel./Fax: +213663815340 ; E-mail address: noudjoud.lebga@univ-bba.dz
DOI: https://doi.org/10.58452/jpcr.v1i2.23

Article history
Received March 29, 2022
Accepted for publication June 20, 2022

Abstract

First principles calculations of the second and third order elastic constants of the cubic silicon carbide β-SiC have been accomplished using the density functional theory within the local density approximation and the pseudopotential plane-wave method with the Hartwigsen Goedecker Hutter scheme. The second order elastic constants C_{ij} compared fairly well with those previously measured by one of us using the Brillouin light scattering technique (P. Djemia) [1]. The ab-initio calculations include parameters pressure dependence determinations in relation with the structural transformation from a zinc Blende to a rocksalt structure. The transition pressure at which arises elastic instabilities is found to be P_t = 113 GPa. Also, we investigate the effects of anharmonicity by calculating the third order elastic constants C_{ijk}. The experimental values are still unknown and comparisons with our calculations are suitable in the future.

Keywords: Silicon carbide; elastic constants, pressure effects, Density Functional Theory (DFT).

1. Introduction

It is well known that there are a large number of polytypes for the SiC crystal whose properties are different for each polytype. Over the last decade, there has been growing interest in the only polytype with a cubic structure 3C-SiC (β-SiC) as a MEMS material. Unlike 6H-SiC, the 3C polytype can be epitaxially grown on single-crystal silicon substrates. At CWRU, the first successful depositions of spatially uniform, single-crystal, 3C-SiC films on 4-inch (100) silicon wafers were made possible. Some of its structural and mechanical properties have been investigated by various techniques [1,3] and will provide us some comparisons with our ab-initio calculations.

In this work, we do first-principle calculations of the second order and third order elastic constants for the silicon carbide zinc blende polytype β-SiC. We compare our numerical results with our experimental available ones [1] and we give prediction for third order elastic constants and pressure dependence of second order elastic constants until the structural transformation from a zinc Blende to a rocksalt structure takes place.

The paper is organized as follows: the computational method is described in section 2. In sections 3 and 4 the results of the calculations of structural and elastic properties are respectively presented and compared with available experimental and theoretical data. In section 5 and 6 the results of the calculations with hydrostatic pressure and of the third order elastic constants are respectively presented. A conclusion is given in section 7.

2. Computational Method

The calculations were performed within the local density approximation LDA to the density-functional theory DFT [4,5], using the pseudopotential plan-wave method as implemented in the ABINIT code [6]. We have used the Teter and Pade parameterization [7] for LDA. Only the outermost electrons of each atom were explicitly considered in the calculation. The effect of the inner electrons and the nucleus (the frozen core) was described within a pseudopotential scheme. We used the Hartwigsen-Goedecker-Hutter scheme [8] to generate the norm-conserving nonlocal pseudopotentials, which results in highly transferable and optimally smooth pseudopotentials. A plane-wave basis set was used to solve the Kohn-Sham equations in the pseudopotential implementation of the DFT-LDA.

The Brillouin zone integrations were replaced by discrete summations over a special set of k-points using the standard k-point technique of Monkhorst and Pack [9] where the k-point mesh used is (8 X 8 X 8). The plane –wave energy cutoff to expand the wave functions is set to be 90 Hartree (1 Hartree = 27.211396 eV).

3. Structural Properties

The minimization of the total energy with respect to the unit cell volume allows us to obtain the equilibrium structural properties of β-SiC. The equilibrium lattice parameter and the bulk modulus can be determined by fitting the total energies calculated at several lattice constants to the Murnaghan's equation of state [10] :

$$E(V)-E(V_0)=\frac{B_0V}{B_0^{'}}\left[\frac{(V_0/V)^{B_0^{'}}}{B_0^{'}-1}+1\right]-\frac{B_0V_0}{B_0^{'}-1} \quad (1)$$

$$B=V\frac{\partial^2E}{\partial V^2}=\frac{4}{9a}\frac{\partial^2E}{\partial a^2} \quad (2)$$

where, at zero pressure, B_0 is the bulk modulus, V_0 is the unit-cell volume, $E(V_0)$ energy at the cell volume and $B_0^{'}=\partial B/\partial P$. Note that another method to compute the equilibrium lattice parameter is the structural optimization using the Broyden-Fletcher-Goldfarb-Shanno minimization (BFGS) [11].

In Table 1, we show the lattice parameter a_0 along with the values of B_0 and $B_0^{'}$; experimental [1,12] and previous theoretical calculations [13,14] are also displayed. We observed that the values of the lattice parameter calculated from the BFGS tool are in good agreement with the ones obtained from

the fits to Murnaghan's equation of the total energies. Moreover, a_0 of SiC agrees quite well with experimental [12] and theoretical [13,14] values.

Table 1. Lattice constant, bulk modulus, elastic constants and their derivative and phase transformation pressure for β-SiC in comparison with experimental [1,12] and other theoretical [13,14] values.
[a] fit to Murnaghan's equation, [b] BFGS and [c] from B= (C_{11}+2 C_{12})/3.

	Our data	Expt	Calc.
a (A°)	4.3355[a]	4.3596 [12]	4.3397 [13]
	4.331[b]		4.36[14]
B_0 (Gpa)	218[a]	225 [12]	218 [13]
	228[c]	**219** [1]	210[a], 216[c] [14]
B_0'	3.599		3.71 [14]

4. Elastic Properties

In a cubic lattice, three independent elastic constants C_{11} , C_{12} and C_{44} are determined by employing suitable lattice distortions. Following the work of Nielsen and Martin [15], we determine these constants. C_{11} and C_{12} can be found from the stress-strain relation with the application of an ε_1 strain. This strain scales the x dimensions by $(1+\varepsilon_1)$ while maintaining constant the y and z dimensions. For small strain the harmonic approximation defines the relations :

$$C_{11} = \frac{\sigma_1}{\varepsilon_1} \tag{3}$$

$$C_{12} = \frac{\sigma_2}{\varepsilon_1} \tag{4}$$

Where σ_i with $(i = 1,2)$ represent the stress.
From the following stress-strain relation [15], one can obtain the elastic constant C_{44}.

$$\sigma_4 = \left[C_{44}^0 - \Omega^{-1}\Phi\left(\xi a_0 / 4\right)^2 \right]\varepsilon_4 = C_{44}\varepsilon_4 \tag{5}$$

In Eq. (5), C°_{44} denotes the elastic constant in absence of internal displacements u , Ω is the volume of the unstrained unit cell, Φ is the force constant and ξ is the internal strain parameter. We can determine C_{44} and ξ with two independent calculations: setting ε_4=0 and a small relative displacement u then with small ε_4 and u=0; details about this method can be found in ref. [15]. The calculations were performed with $\varepsilon_1 = \pm 0.004$ in the direction (100) to determine C_{11} and C_{12} and with $\varepsilon_4 = \pm 0.004$ and $u = \pm 0.002\sqrt{3}a_0$ in the direction (111) to find C_{44}, ξ and the optical Γ-phonon frequency ω_Γ. Φ is the constant force that raise from our results of phonon frequencies and is equal to

$$\Phi = \mu\omega_\Gamma^2 \tag{6}$$

Where μ is the reduced mass.
In Table 2, we show the elastics constants calculated compared with experimental [1,12,16] and previous theoretical calculations [13,14]. The second order elastic constants C_{ij} compared fairly well with those previously measured by one of us using the Brillouin light scattering technique (P. Djemia) [1].

For cubic systems, the bulk modulus *B* can be expressed as a linear combination of the two elastic constants C_{11} and C_{12}:

$$B = \frac{C_{11} + 2C_{12}}{3} \tag{7}$$

The bulk modulus B obtained from Eq. (7) is in reasonable agreement with the values computed by total energy fitting to Murnaghan's equation (1) found earlier (see table 1).

Table 2. Elastic constants and their derivative and phase transformation pressure for β-SiC in comparison with experimental [12,1,16] and other theoretical [13,14] values.

	Our data	Expt	Calc.
C_{11}	402.3 (LDA)	390 [12]	385 [13]
		395±12 [1]	384 [14]
C_{12}	141.1 (LDA)	142 [12]	135 [13]
		132±9 [1]	132 [14]
$(C_{11}-C_{12})/2$	130.5 (LDA)	**136±8** [1]	
C_{44}	253.4 (LDA)	256 [12]	257 [13]
		236±7 [1]	241[[14]
$(C_{11}+C_{12}+2C_{44})/2$	525.1 (LDA)	**504±15** [1]	
ξ	0.413		0.41 [13]
dC_{11}/dp	3.12		3.49 [13]
dC_{12}/dp	3.4		4.06 [13]
dC_{44}/dp	1.32		1.58 [13]
dC^0_{44}/dp	2.75		3.65 [13]
P_t(Gpa)	113.5	100 [16]	65 [14]
V_T/V_0	0.748	0.757 [16]	0.817 [14]

5. Pressure Effect On Elastic Properties

We have calculated the three elastic coefficients C_{11}, C_{12} and C_{44} of β-SiC from the stress-strain relations up to 100 Gpa to study the elastic instability. Both C_{11} and C_{12} increase monotonously with increasing pressure values with a linearly variation for pressure less than 80 GPa, as is shown in fig. 1. On other hand, the variation of C_{44} with the pressure is non-linear one (see figure 1). Analytical relations for the pressure dependence of these elastic constants are given by the quadratic fit below.

$$C_{11} = 408.4+3.44p-0.00365p^2 \tag{8-a}$$
$$C_{12} = 143.8+3.57p-0.00196p^2 \tag{8-b}$$
$$C_{44} = 260.71+1.321p-0.0052p^2 \tag{8-c}$$

For a cubic crystal under pressure p, the generalized elastic stability criteria [17,18] are:

$$K = \frac{1}{3}(C_{11} + 2C_{12} + p) \succ 0 \tag{9-a}$$
$$G' = C_{44} - p \succ 0 \tag{9-b}$$
$$G = \frac{1}{2}(C_{11} - C_{12} - 2p) \succ 0 \tag{9-c}$$

For zero pressure, we find the well-known Born elastic stability criteria [19].
When pressure is applied, SiC transform from zinc-blend phase into rocksalt. We find that G decreases gradually with pressure and vanishes at about 113 GPa and G' decreases also to zero but at higher pressure, as it is shown in fig. 2. Therefore, the phase transition occurs for β-SiC at the much higher pressure at which G becomes zero (P_t=113 GPa). The zinc-blend structure becomes unstable at a volume reduction $V_T/V_0 \approx 0.748$. Where V_0 is the volume at equilibrium and V_T the volume at phase transition.

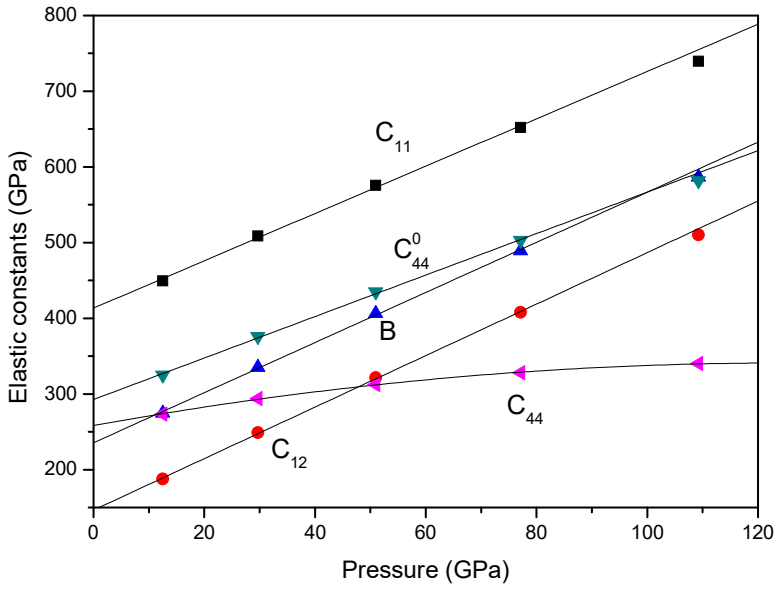

Figure 1. Pressure dependence of the elastic constants for β-SiC. ■ our data, ── fit.

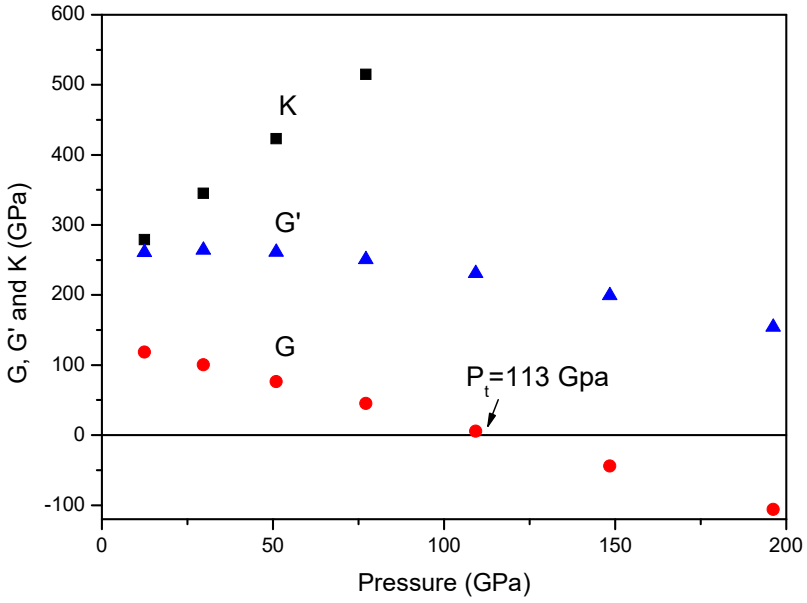

Figure 2. The pressure variation of G, G' and K for β-SiC.

6. Third Order Elastic Constants

Higher-order elastic constants provide an efficient measure of many aspects of lattice anharmonicity. In particular, the third order elastic constants are useful in the calculations of many mechanical and thermal properties related to the anharmonic nature of the lattice potential energy. In addition the third

order elastic constants would be expected to provide useful new information on the nature of cohesive properties and inter atomic forces, so why this constants have received an enormous attention for many materials.

Lattice dynamical models used to model anharmonic properties typically use large numbers of fitting parameters. In contrast, ab-initio methods are inherently free from fitting parameters, thus they usually increase physical insight.

In this part second and third order elastic constants are calculated from the energy variation by applying a strain to the equilibrium lattice configuration. The change in total internal energy per unit of undistorted volume V_0 in response to an applied stress is given by:

$$\frac{\Delta E}{V_0} = \frac{1}{2} C_{ij} e_i e_j + \frac{1}{6} C_{ijk} e_i e_j e_k + ... \tag{10}$$

Where ΔE is the energy increment by the strain vector $e(e_1, e_2, e_3, e_4, e_5, e_6)$ and C_{ij}, C_{ijk} are the matrix of second and third order elastic constants respectively.

For cubic materials, in addition to the three independent C_{ij}, symmetry dictate six independent C_{ijk} $(C_{111}, C_{112}, C_{123}, C_{144}, C_{166}, C_{456})$. This constants were computed using six distortion type labeled I, II, III, IV, V and VI using six component strain notation, distortion I-VI respectively correspond to: uniform dilatation $(e_1 = e_2 = e_3, e_4 = e_5 = e_6 = 0)$; both of [100] and [010] strain $(e_1 = e_2, e_3 = e_4 = e_5 = e_6 = 0)$; distortion at inverse eight $(e_1 = e_2 = -e_3, e_4 = e_5 = e_6 = 0)$, here the phrase constant height refers to constant height of the f.c.c. unit cell ; uniform distortion along [111] $(e_1 = e_2 = e_3 = e_4 = e_5 = e_6)$; [111] shear strain $(e_1 = e_2 = e_3 = 0, e_4 = e_5 = e_6)$ and finally $(e_1 = e_4, e_2 = e_3 = e_5 = e_6 = 0)$ strain.

For the six distortions employed in this study, strain component relate as scalar multiples, adding subscript D to denote the type of distortion while using the above definition of strains I-VI yields the following relationship:

$$\frac{\Delta E_D}{V_0} = \frac{1}{2} k_D e_1^2 + \frac{1}{6} g_D e_1^3 \tag{11}$$

where:

$$k_I = 3C_{11} + 6C_{12} \tag{12-a}$$
$$k_{II} = 2C_{11} + 2C_{12} \tag{12-b}$$
$$k_{III} = 3C_{11} - 2C_{12} \tag{12-c}$$
$$k_{IV} = 3C_{11} + 6C_{12} + 3C_{44} \tag{12-d}$$
$$k_V = 3C_{44} \tag{12-e}$$
$$k_{VI} = C_{11} + C_{44} \tag{12-f}$$

$$g_I = 3C_{111} + 18C_{112} + 6C_{123} \tag{13-a}$$
$$g_{II} = 2C_{111} + 6C_{112} \tag{13-b}$$
$$g_{III} = C_{111} + 6C_{112} - 6C_{123} \tag{13-c}$$
$$g_{IV} = 3C_{111} + 18C_{112} + 6C_{123} + 9C_{144} + 18C_{166} + 6C_{456} \tag{13-d}$$
$$g_V = 6C_{456} \tag{13-e}$$
$$g_{VI} = C_{111} + 3C_{144} \tag{13-f}$$

$k_i, g_i (i = I, II, ...VI)$ are second order force constants and third order force constants respectively.

As is seen from equations (12-a) to (13-f) it is possible to derive the three C_{ij} and the six C_{ijk} from calculation using the sets of strains chosen.

In the present work, 50 sets of $\frac{\Delta E}{V_0}$ for each distortion are obtained from PW-PP calculation by varying the appropriate strains from about -0.5 to about +0.3. The second and third order elastic constants are then obtained from a cubic polynomial fitting of energy strains relation. We have included the following points : all points for distortion type I, II, III;IV for strain type V, $-0.002 \leq e_1 \leq 0.5$; and for strain type VI, $-0.1 \leq e_1 \leq 0.1$. The calculated k_i and g_i are fitted simultaneously and listed in table II with the corresponding third order elastic constants for the β-SiC. The combination of C_{ij} derived from the second order terms are also given in table 3.

Third order elastic constants calculated using the Keating model by Davydov [20] are shown in Table 3. Other second order elastic constants (C_{11} = 410.5 GPa, C_{12} = 164 GPa, C_{44} = 194 GPa) [21] larger than ours were used for his calculations that may explained the large discrepancy between his results and our calculation of C_{ijk}.

Table 3. Calculated second and third-order force constants and the third order elastic constants in units of GPa of β-SiC.

[a] calculated using Eqs (12-a)-(12-f) and the C_{ij} calculated previously.

[b] calculated using Eqs (12-a)-(12-f) and the measured C_{ij} reported in table I.

[c] From Davydov [20] using Keating model and other C_{ij} [21] as input parameters.

	This study		Measured values
K_I	1950.54	2053.5[a]	1977±20[b]
K_{II}	1041.66	1086.8[a]	1054±20[b]
K_{III}	915.28	924.7[a]	921±20[b]
K_{IV}	2748.78	2813.7[a]	2685±28[b]
K_V	813.58	760.2[a]	708±21[b]
K_{VI}	661.16	655.7[a]	631±19[b]
g_I	-17051.17		
g_{II}	-6345		
g_{III}	-6514.92		
g_{IV}	-44391.48		
g_V	-3159.72		
g_{VI}	-1268		
C_{111}	+453.5	-1680[c]	
C_{112}	-906.33	-1026 [c]	
C_{123}	+255.08	-371[c]	
C_{144}	-573.83	3[c]	
C_{166}	-1056.46	-621[c]	
C_{456}	-526.62	-69.5[c]	

Because of the lack in experimental and theoretical value of third order elastic properties of β-SiC, no satisfactory comparison has been made, so why we have calculated the non-linear elastic properties of diamond which are known in order to check the consistency of our calculations. The calculated second and third order force constants are reported in table 4 and show good agreement with known calculated or measured values.

TABLE 4. Calculated second and third-order force constants and in units of GPa of the diamond.

[a] calculated using Eqs. (12-a)-(12-f) and the measured C_{ij} reported in ref [22].

[b] calculated using Eqs. (12-a)-(12-f) and the C_{ij} reported in ref. [23]

[c] calculated using Eqs. (12-a)-(12-f) and the C_{ij} reported in ref [24].

[d] calculated using Eqs. (13-a)-(13-f) and the C_{ijk} reported in ref. [23]

	This study	Measured values	ref. [23]	ref. [24]
K_I	4052	3993[a]	3912[b]	3897[c]
K_{II}	2418	2412[a]	2354[b]	2342[c]
K_{III}	2975	2993[a]	2896[b]	2873[c]
K_{IV}	5763	5730[a]	5562[b]	5499[c]
K_V	1740	1737[a]	1650[b]	1602[c]
K_{VI}	1648.24	1660[a]	1600[b]	1577[c]
g_I	-32982,66		-33300[d]	-54309
g_{II}	-14905,56		-17400[d]	
g_{III}	-12016,56		-11100[d]	
g_{IV}	-86882,52		-87900[d]	
g_V	-6201,18		-7800[d]	
g_{VI}	-3578.7		-6300[d]	

The six second order force constants of diamond calculated using Eq. (12-a) to (12-f) and measured C_{ij} agree well with our results to within 2 %, also our six third order force constants are in good agreement with the one calculated using Eq. (13-a) to (13-f) and the ab-initio C_{ijk} reported in ref [23].

The procedure applied in the case of diamond has been employed for the β-SiC, but in view of the limited experimental and theoretical value no valuable comparison has been made and we suggest that the C_{ij} and C_{ijk} in table II are predictions to be verified by future experiments.

7. Summary And Conclusions

We have performed high pressure ab-initio calculations of the elastic properties for the zinc blende polytype of silicon carbide β-SiC. the results obtained of the elastic constants (C_{11}, C_{12}, and C_{44}),are in good agreement with the available experimental and theoretical data reported in the literature.

The pressure at which the transition from zinc-blende to Rocksalt structure should arise is found to be 113 GPa and is associated to the elastic instability $\left(C_{11}-C_{12}-2p\right)=0$. Our results predict the pressure dependence of the three independent elastic constants (C_{11}, C_{12}, C_{44}) for β-SiC that still have not been experimentally derived.

Also, we investigate the effects of anharmonicity by calculating the third order elastic constants C_{ijk}. Because of the lack in experimental and theoretical value of third order elastic properties no comparison has been made. Then, further experiments are suitable.

References:

[1] P. Djemia, Y. Roussigné, G. F. Dirras, K. M. Jackson. J. Appl. Phys. **95** (2) (2004) 2324-2330.
[2] P. Masri, , N. Moureaud, M. Rouhani Laridjani, J. Calas, M. Averous, G. Chaix, A. Dollet, R. Berjoan, C. Dupuy, Materials Science and Engineering B, **61-62,** (1999), 535-538
[3] K. M. Jackson, Sensors and Actuators A, **125,** (2005), 34-40.
[4] P. Hohenberg, W. Kohn, (1964), Phy Rev. B, **136**, 864
[5] W. Kohn, L. J. Sham, Phy Rev. A, **140**, (1965), 1133
[6] The ABINIT computer code is a common project of the Universite Catholique de Louvain, Corning Incorporated, and other contributors. (URL http: //www.abinit.org)
[7] Teter Pade fitting of PW92 data: see the appendix of S. Goedecker, M. Teter, and J. Hutter, Phys. Rev. B, (1996), **54**, 1703; J.P. Perdew, K. Burke, and M. Ernzerhof, Phys. Rev. Lett. **77**, (1996), 3865
[8] C. Hartwigsen, S. Goedecker, J. Hutter, Phys. Rev. B **58** (1998) 3641
[9] H. J. Monkhorst, J. D. Pack, Phys. Rev. B, **13**, (1976), 5189
[10] F D. Murnaghan, Proc, Natl Acad, Sci, USA, **30,** (1944), 244
[11] C. G. Broyden, Journal of the Institute for Mathematics and Applications, Vol. **6**, (1970), 222-231, R. Fletcher, Computer Journal, Vol. **13**, (1970), 317-322. D. Goldfarb, Mathematics of Computation, Vol. **24**, (1970), 23-26. D. F. Shanno, Mathematics of Computation, Vol. **24**, (1970), 647-656. See also summary in: D. F. Shanno, Journal of Optimization Theory and Applications, Vol.**46**, No 1, (1985), 87-94.
[12] W.R.L. Lambrecht, B. Segal, A. Methfessel, M. Schilfgaard, phys. Rev. B, **44**, (1991), 3685
[13] M. Prikhodkho, M. S. Miao, W.R.L. Lambrecht, Phys. Rev. B, **66**, (2002), 125201
[14] Cheng-Zhang Wang, Rici Yu, Henry Krakauer, Phys. Rev. B, **53 (9),** (1996), 5430- 5437
[15] O. H. Nilssen, R. M. Martin, Phy. Rev. B, **32**, (1985), 3792.
[16] M. Yoshida, A. Onodera, M. Ueno, K. Takemura, O. Shimomura, Phys. Rev. B **48**, (1993), 10 587
[17] Sidney Yip, J. Li, M. Tang, J. Wang, Materials Science and Engineering **A, 317**, (2001), 236-240
[18] G.V. Sinko, A. Smirnov, J. Phys. Condens. Matter, **14**, (2002), 6989
[19] M. Born and K. Huang: Dynamical Theory of Crystal Lattices, Oxford: Clarendon. 1954
[20] S. Yu. Davydov, Physics of the Solid State, **46** (7), (2004), 1200-1205.
[21] S. P. Nikanorov, B. K. Kardashev: Elasticity and Dislocation Inelasticity of Crystals, Nauka, Moscow. (1985)
[22] H. McSkimin, P. Andreatch, P. Glynn, J. Appl. Phys., **43,** (1972), 985.
[23] O. H. Nielsen, Phys. Rev. B., **34**, (1986), 5808
[24] D.G. Clerc, H. Ledbetter, journal of Physics and Chemistry of Solids, **66 ,** (2005), 1589

J. Phys. & Chem. Res. **1**, Issue 2, December (2022) 25–30

Journal of Physical & Chemical Research

Journal homepage: https://ojs.univ-bba.dz

Hydrostatic pressure effect on the structural parameters of GaSb semiconducting material: *Ab-initio* calculations

Farouk Bengasmia[1], Ammar Benamrani[1*], Lotfi Boutahar[2], Hamza Rekab-Djabri[3,4], Salah Daoud[2]

[1]*Faculty of Sciences and Technology, Mohamed El Bachir El Ibrahimi University of Bordj Bou Arreridj, 34000 Bordj Bou Arreridj, Algeria*
[2]*Laboratory of Materials and Electronic Systems, Faculty of Sciences and Technology, Mohamed El Bachir El Ibrahimi University of Bordj Bou Arreridj, 34000 Bordj Bou Arreridj, Algeria.*
[3]*Laboratory of Micro and Nanophysics (LaMiN), Oran ENP, BP 1523, El M'Naouer, 31000, Oran, Algeria*
[4]*Faculty of Nature and Life Sciences and Earth Sciences, Akli Mohand-Oulhadj University, 10000, Bouira, Algeria*

* Corresponding author: Tel./Fax: +0-000-000-0000 ; E-mail address: ammar.benamrani@univ-bba.dz
DOI: https://doi.org/10.58452/jpcr.v1i2.24

Article history
Received 4 April, 2022
Accepted for publication 13 November, 2022

Abstract

Ab-initio calculations were performed to investigate the ground state and hydrostatic pressure effect on the structural properties of GaSb semiconducting material. The projected augmented wave pseudopotentials (PAW) approach in the framework of the density functional theory (DFT) as implemented in the Quantum Espresso code was used. The exchange-correlation functional was described with the generalized gradient approximation (GGA). Utilizing the energy - volume (E-V) data, our values of the equilibrium lattice constant, the bulk modulus, and the pressure derivative of the bulk modulus of GaSb semiconductor obtained from the Birch–Murnaghan equation of state were found 6.220 Å, 44.84 GPa and 4.22, respectively. Our obtained data agree well with the available experimental values and other theoretical data of the literature. In addition, the melting point, the lattice thermal expansion coefficient and the microhardness of our material of interest were also calculated and compared with the available experimental data of the literature.

Keywords: III-V semiconducting materials, Ab-initio calculations, structural parameters, melting point.

1. Introduction

III–V semiconducting materials are made from group III and V elements of the Mendeleev table (the periodic table) [1-4]. III–V compounds are technologically important materials due to their versatile technological usage and flexibility of their physical properties *via* structural engineering, they have been extensively served as substances for electronic and optoelectronic devices [3].
Among III–V semiconducting compounds, the antimonide based compound. At ambient pressure and temperature, III-Sb semiconducting compounds crystallize in the cubic zincblende (ZB) structure. Boron antimonide (BSb) and aluminium antimonide (AlSb) have indirect band gap, while gallium antimonide (GaSb) and indium antimonide (InSb) have direct ones [3].
Recently, GaSb semiconducting compound is considered as promising material for potential applications in field-effect transistors (FET), lasers, multi-junction solar cells (MJSC), infrared detectors (ID), and Shockley diodes [5]. At ambient pressure and temperature, GaSb compound is a

direct semiconductor with a narrow band gap of *Eg* = 0.725 eV [5], a lattice constant is equal to 6.096 Å, a crystal density of 5.615 g/cm^{3}and its melting point of 991 K [6].
Using, full-potential linearized augmented plane wave (FP-LAPW) method, Moussa *et al.* [5] investigated the structural parameters, electronic and optical properties, and elastic constants of cubic $Al_xGa_{1-x}Sb$ ternary alloys. They found that the band gap variations with the composition of the ternary alloys exhibit a small deviation from the Vegard's law, and the obtained results confirm the semiconducting character of the studied materials. Besides, they found that the lattice parameter of the $Al_xGa_{1-x}Sb$ alloys showed a non-linear variation with the Aluminum mole fraction.
In this investigation, we focus on studying the effect of the hydrostatic pressure on the structural properties of GaSb material. Firstly, we explain the method of calculation used in our work; secondly, we present and discuss the results obtained; and finally, we finish with a brief conclusion.

2. Method of calculations

In the present work, the Quantum Espresso code with Thermo_PW tool [7-9] were employed to investigate the effect of hydrostatic pressure on the structural properties of GaSb semiconducting material. The Quantum Espresso code is based on the pseudopotential (PP) method and a plane waves basis set. The Ga.pbe-dn-kjpaw_psl.1.0.0.UPF and Sb.pbe-dn-kjpaw_psl.1.0.0.UPF projector augmented wave pseudopotentials (PAW) [10] are used for gallium (Ga) and antimony (Sb) atoms, respectively. As it is well known, the term of exchange and correlation (XC) is not known exactly, therefore, the exchange-correlation potential was calculated using the Perdew-Burke-Ernzerh of generalized gradient approximation (PBE-GGA) [11]. The PBE-GGA functional do not express the XC energy density only as a function of the local density (LD), but it takes into account its gradient.
In the present work, the wave functions were expanded with an energy cut-off of 70 Ry for the plane wave basis set; while the charge density cut-off was taken equal to 700 Ry. The integration over the Brillouin zone was performed using 6x6x6 k-points Monkhorst-Pack mesh [12].With these previous conditions, a convergence with an energy threshold of $1x10^{-4}$ Ry was achieved.

3. Resultsand discussions

3.1. Equilibrium structural parameters

One of the major problems in geophysics science, materials science, and condensed matter physics is the determination of the equation of state and the other thermodynamic properties of materials [13]. As it was mentioned previously, GaSb semiconducting compound crystallizes in the cubic zincblende (B3) structure. The unit cell geometry of B3 phase was assigned as: $a = b = c$ (lattice constants), and $\alpha = \beta = \gamma = 90°$ (lattice angles). In B3 structure, the material is constituted of two different atoms per basis (molecule), with a unit cell of 8 atoms (4 atoms of III element (Ga), and 4 atoms of V element (Sb)) (see Fig. 1) [14], while, the wurtzite (B4) lattice has only four atoms (two molecular units) in the primitive unit cell [6].

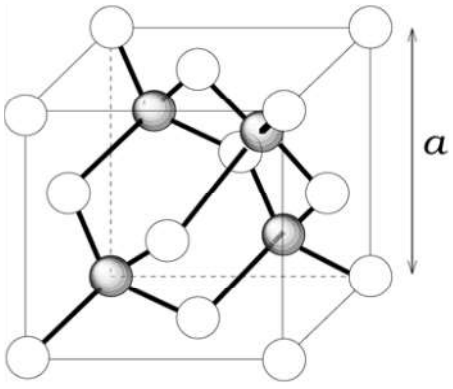

Figure 1. Cubic zincblende (B3) crystal structure for III-V semiconducting material [14].

The energies were obtained by hydrostatic compression / dilation of the unit cells. Figure 2 shows the evolution of the total energy as a function of the unit cell volume of cubic zincblende GaSb material.

From the total energy E_{Tot} presented as a function of the cell volume V, one can deduce the static structural parameters, such as the equilibrium lattice constant a_0 from the volume which gives the minimum energy, the bulk modulus B_0 and the derivative of the bulk modulus with respect to pressure B_0' by fitting the total energy with the Birch-Murnaghan's equation of state (BM-EOS), which is expressed as follows [15]:

$$E(V) - E_0 = \frac{9V_0B_0}{16}\left\{B_0'\left[\left(\frac{V_0}{V}\right)^{2/3} - 1\right]^3 + \left[\left(\frac{V_0}{V}\right)^{2/3} - 1\right]^2\left[6 - 4\left(\frac{V_0}{V}\right)^{2/3}\right]\right\} \quad (1)$$

where, V_0 is the equilibrium unit-cell volume, and E_0 is the corresponding energy.

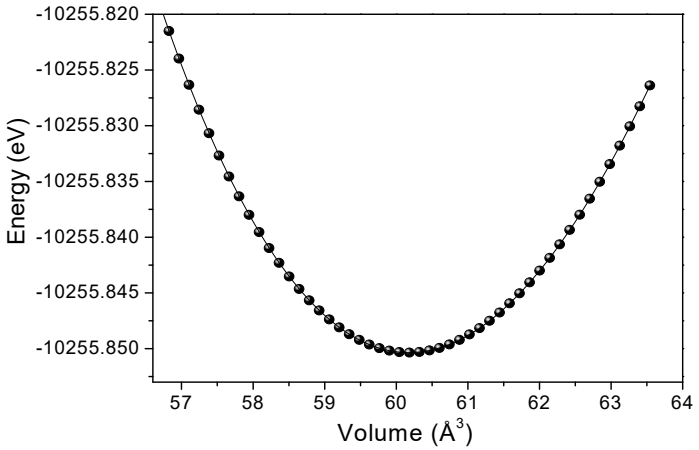

Figure 2. Total energy versus the primitive unit cell volume for cubic zincblende (B3) GaSb.

Our calculated values of the equilibrium lattice constant a_0, the bulk modulus B_0, and its pressure derivative B_0' for GaSb material are summarized in Table. 1, in comparison with the experimental data [6, 16, 17] and other theoretical results [18, 19]. Although our value (44.84 GPa) of B_0 is slightly lower than the experimental data one 56.31 GPa reported in Ref. [6], there is a strong evidence that our calculated values of a_0, and B_0' coincide well with experimental data [6, 16, 17] and other theoretical results [18, 19]. The deviation between our calculated value (6.220 Å) of the lattice constant a_0 and the experimental result (6.130 Å) reported by Böer and Pohl [16] is only around 1.47%.

Table 1. Optimized equilibrium structural parameters a (Å), the bulk modulus B_0 (GPa), and pressure derivative of bulk modulus B'_0 for GaSb semiconducting material.

Parameter	Our data	Experimental data	Other calculations
a_0(Å)	6.220	6.096 [6], 6.130 [16]	6.005 [18], 5.981 [19]
B_0 (GPa)	44.84	56.31 [6], 55.4 [17]	56 [18], 56.7 [19]
B'_0	4.22	4.78 [6]	4.64 [18], 4.662 [19]

The melting temperature T_m and the Debye temperature θ_D are two fundamental thermophysical properties of materials [4, 20]. The melting temperature T_m is one of the important information required for the thermal characterization of materials [21]. The melting point T_m of several solids having a cubic structure correlates with the bulk modulus B by this empirical formula [22, 23]: T_m= 9.3B + 607, where T_m is expressed in K, and B is expressed in GPa. Although several empirical expressions are not supported by fundamental theory, much important information of semiconducting materials have been obtained on the basis of these equations. Replacing our value (44.84 GPa) of the bulk modulus B_0 in the previous equation, the melting point T_m of GaSb material was found equal to 1024 K. This value is slightly higher than the experimental value 991 K reported by Adachi [6]. The deviation between our value (1024 K) of T_m and the result (991 K) [6] is only around 3.33%.

For binary tetrahedral semiconductors, the lattice thermal expansion coefficient α in (10^{-6} K^{-1}) is given by this relation [24]: $\alpha = k(T_m \times Z_1Z_2)^{-1/2}$-$d^{1/2}$, where T_m is the melting temperature in K, Z_1 and Z_2 are ionic charge of cation and anion, respectively, d ($d = 0.25\sqrt{3}a$) is the nearest-neighbour distance in Å, and k is dimensionless constant. The value of constant k for cubic zincblende type crystal structure is

775 [24]. Replacing our values 1024 K of T_m and 2.69 Å of d in the previous equation, the lattice thermal expansion coefficient α of GaSb material was found equal to 6.43×10^{-6} K^{-1}. This value is in excellent agreement with the experimental value (6.5×10^{-6} K^{-1}) reported by Van Uitert [25]. The deviation between our value (6.43×10^{-6} K^{-1}) of α and the experimental one (6.5×10^{-6} K^{-1}) reported by Van Uitert [25] is less than1.1%.

Daoud [4] has shown that for many II–VI and III–V semiconductors having tetrahedral structure, the Debye temperature θ_D is roughly proportional to the bond-length d, they are related by:

$$\theta_D = K_3 \, [1/(M^{1/2} d^{5/4})] - K_4 \qquad (2)$$

where d is expressed in 10^{-10} m, M is the molar mass, and K_3 and K_4 are two empirical parameters (for group III–V, $K_3 = 112.66$ (10^{-12} $Kg^{1/2}$ $m^{5/4}$ K) and $K_4 = 90.74$ K, respectively).

Replacing our value (2.693×10^{-10} m) of d in the previous equation, the Debye temperature θ_D of GaSb was found equal to 243 K. Although our data of θ_D is slightly lower than the value 266 K obtained at low-temperature ($T = 0$ K) [6], it is in good agreement with the experimental one 240 K measured at T = 273 K [6], and other theoretical ones (233 K, 302 K, and 331 K) reported by Narain [26]. Our value (243 K) of θ_D deviates from the value (240 K) reported by Adachi [6] by only around 1.25%.

For groups II–VI and III–V, semiconductors having tetrahedral structure, and based on the plasma oscillations theory of solids, Bahadur and Mishra [27] developed an empirical relation for the calculation of the microhardness H, which is given as follows: $H = \beta \, r_S^{-5.57}$ [27], where β is a constant, (its numerical value is 365.86 for III–V group), and the electron density parameter r_s is expressed as follow: $r_s = 1.388 \, a_0 \left(W/Z' \rho\right)^{1/2}$ [27], where a_0 is the Bohr radius, W is the molecular weight of the compound, Z' is the effective number of electrons taking part in the plasma oscillation, and ρ is the density. The electron density parameter r_S and the bond-length d are also related by: $d = 1.173 r_S$ [27]. Using the previous expressions, the microhardness H of GaSb was found equal to 3.57 GPa, which is slightly lower than the experimental values 4.48–4.68 GPa reported by Adachi [6].

3.2. Hydrostatic pressure effect

The study of equation of state means the investigation of pressure, volume and temperature (P–V–T) relation. The study of equation of state (EOS) facilitates to know about the nature of solid state theories [28]. EOS also helps us to determine the values of fundamental thermodynamic parameters of semiconducting compounds and other materials [28]. In order to show how the structural parameter in GaSb compound behaves under external pressure, the volumes of the primitive unit cell were computed at fixed values of applied hydrostatic pressure in the range of 0 to 3.5 GPa. Fig. 3 shows the variation of the primitive unit cell volume V of GaSb as a function of pressure p. The fit of our data regarding the volume V as a function of p obeys the following polynomial expression: $V = 60.18 - 1.33p + 0.06p^2$, where V is expressed in $Å^3$, and p is expressed in GPa.

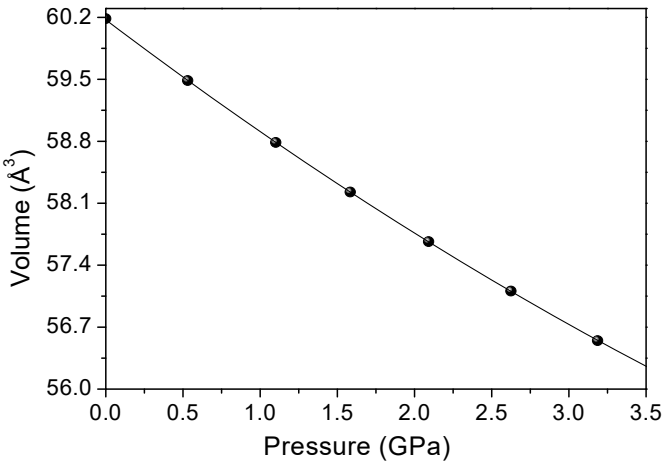

Figure 3. Primitive unit cell volume versus pressure for GaSb semiconducting material.

The crystal density ρ of material is related to the atomic arrangement and corresponding electron density map [6]. The crystal density ρ can be calculated as follows [29-31]:

$$\rho = ZM/N_A V \quad (3)$$

where Z is the number of molecules per unit cell, M is the molecular weight, N_A is the Avogadro constant, and V is the volume of unit cell (for binary compounds which crystallizes in the cubic zincblende (B3) structure ($V = a^3$)). The pressure dependence of the crystal density ρ for GaSb material was offered in Fig. 4. From curve of Fig. 4, we observe clearly that the crystal density ρ of GaSb semiconducting material increases with increasing of pressure. Similar qualitative behaviors have been reported for the crystal density ρ versus pressure for cubic zinc-blende AlP semiconducting compound [3], $B_xAl_{1-x}Sb$ ternary alloys [22], (B2-type) Yttrium-Rhodium (YRh) rare earth intermetallic compound [32], cubic zinc-blende thallium phosphide (TlP) compound [33], and cubic zinc-blende boron phosphide (BP) compound [34]. The crystal density ρ of GaSb material started with the value 5.283 g/cm^3 at zero-pressure, and it reaches the value of 5.652 g/cm^3 at 3.5 GPa. At zero-pressure, our value of ρ is around 5.283 g/cm^3, it is slightly lower than the experimental one (5.615 g/cm^3) reported by Adachi [6]. The fit of our data regarding the crystal density ρ as a function of pressure p obeys the following expression: $\rho = 5.284 + 0.118p - 3.45\times10^{-3}p^2$, where ρ is expressed in g/cm^3, and p is expressed in GPa.

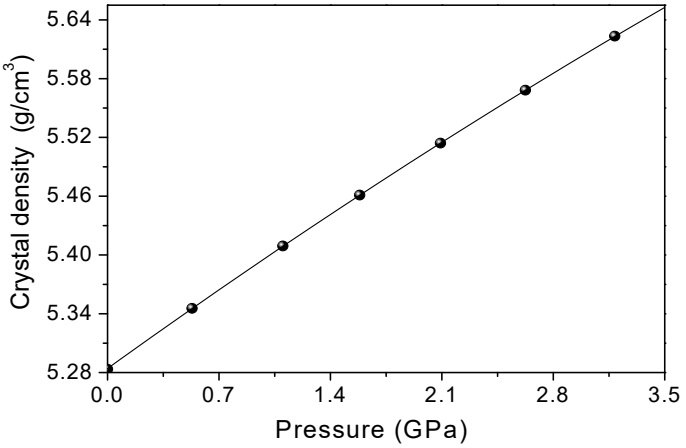

Figure 4. Crystal density versus hydrostatic pressure for cubic zincblende (B3) GaSb.

A second way was usually used to present the effect of the compressional behavior on the physical quantities, i.e as a function of the normalized lattice constant (a/a_0) [35]. The crystal density ρ of GaSb for different values of (a/a_0) is displayed in Fig. 5. The fit of our data regarding the crystal density ρ as a function of a/a_0 obeys the following polynomial expression: $\rho = 54.52 - 82.63\ (a/a_0) + 33.40\ (a/a_0)^2$, where a/a_0 is dimensionless (without unity), and ρ is expressed in g/cm^3.

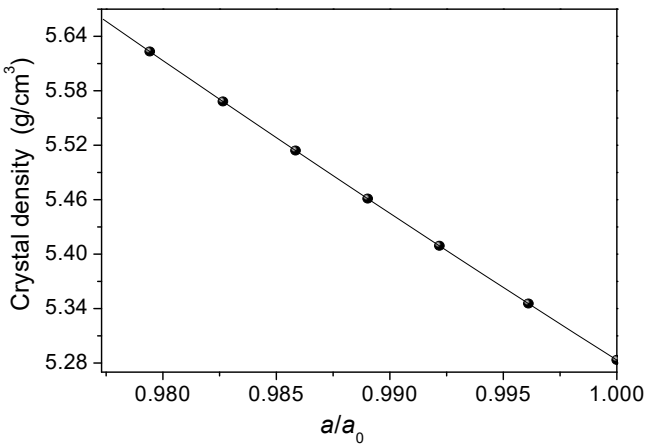

Figure 5. Crystal density versus normalized lattice constant a/a_0 for GaSb compound.

4. Conclusion

In this study, the equilibrium structural parameters as well as the effect hydrostatic pressure on the crystal density of the cubic GaSb semiconducting material were investigated using the projected augmented wave pseudopotentials (PAW) approach in the frame work of the DFT. In general, our calculated structural parameters agree well with other data of the literature. Our calculated value (6.220 Å) of a_0 deviates from the experimental one (6.130 Å) by only around 1.47%.
In addition, the melting temperature T_m, the Debye temperature, the linear lattice thermal expansion coefficient α, and the microhardness of our material of interest were also calculated. The data obtained in this work are in good agreement with the experimental values of the literature. Our value (1024 K) of T_m deviates from the experimental result (991 K) by about 3.33%, while our predicted data (6.43 x 10^{-6} K^{-1}) of α deviates from the experimental one (6.5 x 10^{-6} K^{-1}) by less than 1.1%. These marked results signify the good values obtained for the structural parameters.

References

[1] S. Daoud, N. Bioud, N. Lebga, R. Mezouar, Int. J. Phys. Res.**2** (2014) 27–31.
[2] H. Salehi, H. Badehian, M. Farbod, Mat. Sci. Semicon. Proc. **26** (2014) 477–490.
[3] S. Daoud, N. Bioud, N. Lebga, J. Optoelectron. Adv. Mater. **16** (2014) 207–214.
[4] S. Daoud, Int. J. Sci. World. **3** (2015) 275–279.
[5] R. Moussa, A. Abdiche, R. Khenata, F. Soyalp, Opt. Mater.**113** (2021) 110850.
[6] S. Adachi,*Properties of Group-IV, III-V and II-VI Semiconductors*, John Wiley & Sons Ltd (2005).
[7] S. Baroni, A. DalCorso, S. deGironcoli, P. Giannozzi, Rev. Med. Phys. **73** (2001) 515–562.
[8] S. Scandolo, P. Giannozzi, C. Cavazzoni, S. deGironcoli, A. Pasquarello, S. Baroni, Z. Kristallogr. **220** (2005) 574–579.
[9] A. Dal Corso, J. Phy. Condens. Matter. **28** (2016) 075401. See *https://dalcorso.github.io/thermo_pw/*
[10] P.E. Blöchl, Phys. Rev. B **50** (1994)17953–17979.
[11] J.P. Perdew, K. Burke, M. Ernzerhof, Phys. Rev. Lett. **77** (1996) 3865–3868.
[12] H.J. Monkhorst, J.D. Pack, Phys. Rev. B**13** (1976) 5188–5192.
[13] A. Benmakhlouf, A. Benmakhlouf, O. Allaoui, S. Daoud, Chinese J. Phys. 57 (2019) 179–188.
[14] S. Daoud, N. Bioud, Ukr. J. Phys. **59** (2014) 418–425.
[15] F. Birch, Phys. Rev.**71** (1947) 809–824.
[16] K.W. Böer, U.W. Pohl, *Semiconductor Physics*, Springer International Publishing AG, Switzerland (2018).
[17] S. Muramatsu, M. Kitamura, J. Appl. Phys. **73** (1993) 4270–4272.
[18] T. K. Gajaria, S. D. Dabhi, P. K. Jha, Scientific Reports.**9** (2019) Art. Number 5884.
[19] S. Q. Wang, H. Q. Ye, J. Phys. Condens. Matter.**14** (2002) 9579–9587.
[20] S. Daoud, Int. J. Sci. World. **5** (2017) 9-12.
[21] S. Daoud, N. Bouarissa, A. Benmakhlouf, O. Allaoui, Phys. Status Solidi B **257** (2020) 1900537 (11pp).
[22] T. Özer, Can. J. Phys. **98** (2020) 357-363.
[23] S. Daoud, P.K. Saini, H. Rekab-Djabri, J. Nano- Electron. Phys.**12 No 6** (2020) 06008 (5pp).
[24] A. S. Verma, R.K. Singh, S. K. Rathi, Physica B **404** (2009) 4051–4053
[25] L.G. Van Uitert, Mater. Res. Bull. **12** (1977) 315–320.
[26] S. Narain, Phys. Status Solidi B **182** (1994) 273-278.
[27] A. Bahadur, M. Mishra, J. Res. Phys. **36** (2012) 31-42.
[28] P. Bhardwaj, S. Singh, Mater. Sci. Semicond. Process. **31** (2015) 44–51.
[29] S. Daoud, A. Latreche, Indian J. Phys.**90** (2016) 1243–1244.
[30] A. Latreche, S. Daoud, Trans. Indian Inst. Met. **70** (2017) 1159 –1160.
[31] H. Rekab-Djabri, Manal M. Abdus Salam, S. Daoud, M. Drief, Y. Guermit, S. Louhibi-Fasla, J. Magnes. Alloys, **8** (2020)1166–1175.
[32] A. Benamrani, S. Daoud, Manal M. Abdus Salam, H. Rekab-Djabri, Mater. Today Commun. **28** (2021) 102529.
[33] S. Daoud, N. Bioud, Int. J. Phys. Res.**2** (2014) 50–55.
[34] S. Daoud, K. Loucif, N. Bioud, N. Lebga, L. Belagraa, Pramana – J. Phys.**79** (2012) 95–106.
[35] S. Labidi, H. Meradji, S. Ghemid, S. Meçabih, B. Abbar, J. Optoelectron. Adv. Mater. **11** (2009) 994-1001.

Journal of Physical & Chemical Research

Journal homepage: https://ojs.univ-bba.dz

Calcul empirique du rapport d'intensité (K_β/K_α) pour les élements lègers de $_{11}$Na à $_{30}$Zn

Salim Daoudi[1,2*], Houria Rakhroukh[1], Yazid Kasri[3], Abdelhalim Kahoul[1,2]

[1] *Department of Matter Sciences, Faculty of Sciences and Technology, Mohamed El Bachir El Ibrahimi University, Bordj-Bou-Arreridj 34030, Algeria*
[2] *Laboratory of Materials Physics, Radiation and Nanostructures (LPMRN), University of Mohamed, El Bachir El Ibrahimi, Bordj-Bou-Arreridj 34030, Algeria*
[3]*Theoretical Physics Laboratory, Physics Department, University of Bejaia, 06000 Bejaia, Algeria.*

* *Corresponding author*: S. Daoudi . *E-mail address: s.daoudi@univ-bba.dz*
DOI: https://doi.org/10.58452/jpcr.v1i2.25

Article history
Received April 08, 2022
Accepted for publication July 14, 2022

Abstract

Dans ce travail, sur la base des données expérimentales publiées dans la littérature, nous proposons une fonction analytique qui permettra de déduire les valeurs empiriques du rapport d'intensité K_β/K_α pour des éléments de Z = 11 à 30. Les résultats obtenus ont été présentés sous forme tabulaire et ont été comparés aux travaux théoriques, empiriques et expérimentaux.

Keywords: Rapport d'intensité K_β/K_α, calcul empirique, elements lèges.

1. Introduction

Les rapports d'intensité K_β/K_α sont des quantités importantes en spectroscopie nucléaire et en physique atomique. Ces quantités ont été résumées dans plusieurs articles de synthèse dans différents domaines de recherche. L'étude de ces paramètres pour les éléments du tableau périodique a fait l'objet de plusieurs travaux expérimentaux et également des études théoriques, en vue de leurs applications pour l'analyse élémentaire non-destructive en physique médicale, chimie des surfaces, sciences de l'environnement et de l'industrie. Dans ce travail on a proposé une simple fonction analytique basée sur les données expérimentales compilées par Daoudi et al. [1] pour calculer les valeurs empiriques du rapport d'intensité K_β/K_α pour des éléments compris entre Z= 11 et Z= 30. Les résultats obtenus ont été présentés sous forme tabulaire et ont été comparés à des travaux théoriques, empiriques et expérimentaux. Les valeurs mesurées du rapport K_β/K_α d'intensité induites par les photons publiées dans la littérature de la période 1969 – 2018 (127 articles de 1118 valeurs) ont été présentées par Daoudi et al. [1] pour les éléments atomiques de $_{11}$Na à $_{96}$Cm, un examen critique de ces données à l'aide des valeurs moyennes pondérées $(K_\beta/K_\alpha)_w$ a été effectué pour chaque élément et des valeurs pondérées recommandées ont été proposés.
Le tableau du "meilleur" rapport du taux d'émission des rayons X (K_β/K_α, $K_{\beta2'}/K_{\alpha1}$, $K_{\beta1'}/K_{\alpha1}$, $(K_{\beta1}+K_{\beta3})/K_{\alpha1}$, $K_{\beta3}/K_{\beta1}$ et $K_{\alpha2}/K_{\alpha1}$) a été présenté par Nelson et al. [2], en traçant des courbes sur la base des données expérimentales publiées à cette époque pour les éléments atomiques $20\leq Z\leq100$. Salam et al. [3] ont calculé les valeurs les plus probables du rapport d'émission de rayons X (K_β/K_α, $K_{\beta3}/K_{\beta1'}$, $K_{\beta5}/K_{\alpha1}$, $K_{\beta4}/K_{\alpha1}$, $K_{\beta2'}/K_{\alpha1}$, $K_{\beta1}/K_{\alpha1}$, $K_{\alpha3}/K_{\alpha1}$ et $K_{\alpha2}/K_{\alpha1}$) pour les éléments $12\leq Z\leq100$ par la

méthode d'interpolation des moindres carré. Scofield dans son célèbre article [4] a calculé les rapports d'émission des rayons X (K_β/K_α, $K_{\alpha2}/K_{\alpha1}$, $K_{\beta3}/K_{\beta1}$, $K_{\beta1}/K_{\alpha1}$,$K_{\beta1'}/K_{\alpha1}$, $K_{\alpha3}/K_{\alpha1}$, $K_{\beta1}/K_{\alpha1}$, $K_{\beta1}/K_{\beta1}$ et $K_{\beta5}/K_{\beta1}$) basés sur la théorie Hartree-Slater- relativiste pour les éléments $5\leq Z\leq 104$.
Les valeurs mesurées du rapport d'intensité K_β/K_α publiées dans la littérature de 1980 à 2011 (41 articles et 369 valeurs) ont été rapportées par Kahoul et al. [5] pour des éléments avec $16\leq Z\leq 92$, ensuite les valeurs moyennes pondérées et non pondérées des données expérimentales ont été ajustées par une fonction analytique pour déduire de nouveaux rapports d'intensité K_β/K_α semi-empiriques et empiriques pour un certain nombre d'éléments allant de Z = 16 à 92.

2. Méthode

Les méthodes de calcul des sections efficace de production de rayon X, des rapports d'intensités, des probabilités de transfert entre les couches. Les rapports d'intensité radiatives, expérimentales et analytiques sont très importantes en raison du grand nombre de leurs applications dans divers domaines chimiques, physiques et médicales. Plusieurs études ont été réalisées pour mesurer et calculer ces valeurs sur tous les éléments du tableau périodique.
Premièrement, pour calculer empiriquement K_β/K_α pour les éléments de l'intervalle $11\leq Z\leq 30$, nous avons présenté la quantité des données expérimentales réduites $\left(\left(K_\beta/K_\alpha\right)_{exp}/\left(1-\left(K_\beta/K_\alpha\right)_{exp}\right)\right)^{1/4}$ en fonction du numéro atomique Z, avec $(K_\beta/K_\alpha)_{exp}$ sont les valeurs expérimentales tirées des différentes publications. Ces données expérimentales réduites en function de Z sont présentées sur la figure 1.
Deuxièmement, nous avons proposé une function analytique polynômiale pour interpoler cette quantité. La fonction analytique utilisée pour l'interpolation est la suivante:

$$\left(\frac{\left(K_\beta/K_\alpha\right)_{exp}}{1-\left(K_\beta/K_\alpha\right)_{exp}}\right)^{1/4} = f(Z) = \sum_i b_i Z^i \quad (1)$$

Cette fonction est ullistrée par une ligne continue sur la figure 1.
Pour déduire les valeurs empiriques du rapport d'intensité (K_β/K_α) pour les éléments de numéros atomique $11\leq Z\leq 30$, nous avons utilisé la formule ci-dessous:

$$\left(K_\beta/K_\alpha\right)_{exp} = \left(\frac{f^4(Z)}{1+f^4(Z)}\right) \quad (2)$$

Avec f(Z) est un polynôme determiné par la méthode des moindres carrés:

$$f(Z) = -1{,}07447 + 0{,}19005 \times Z - 0{,}00709 \times Z^2 + 8{,}80055 \times 10^{-5} \times Z^3 \quad (3)$$

3. Résultats et discussion:

Le présent calcul des rapports d'intensités K_β/K_α empirique pour touts les éléments dans la région $11\leq Z\leq 30$ est présenté dans le tableau 1. Les valeurs théoriques de Scofield [4], les résultats d'interpolation de Salam et al. [3], Kahoul et al. [5], Khan and Karimi [6], et les mesures expérimentales de Kararsiz [7], Chang et al. [8] and Öz [9], sont aussi ajoutés dans le même tableau. Les figures 2, 3 et 4 montrent la comparaison de nos résultats empiriques obtenues des rapports d'intensités avec ceux des valeurs théoriques, interpolés et expérimentales en fonction du nombre atomique Z.
Nous observons qu' en général , les rapports d'intensités calculés en utilisant la formule (3) sont conformeS aux valeurs théoriques, interpolées et expérimentales des autres auteurs. La figure 2 montre que nos données diffèrent par un petit pourcentage en comparaison avec les valeurs théoriques de Scofield [4] dans la zone des elements atomiques avec $18\leq Z\leq 30$. L'écart entre les deux séries de valeurs varie entre 4.14% à 10.10%. Pour les elements de $11\leq Z\leq 17$, on observe un écart important qui attaint la valeur 73.31% pour Z=11.

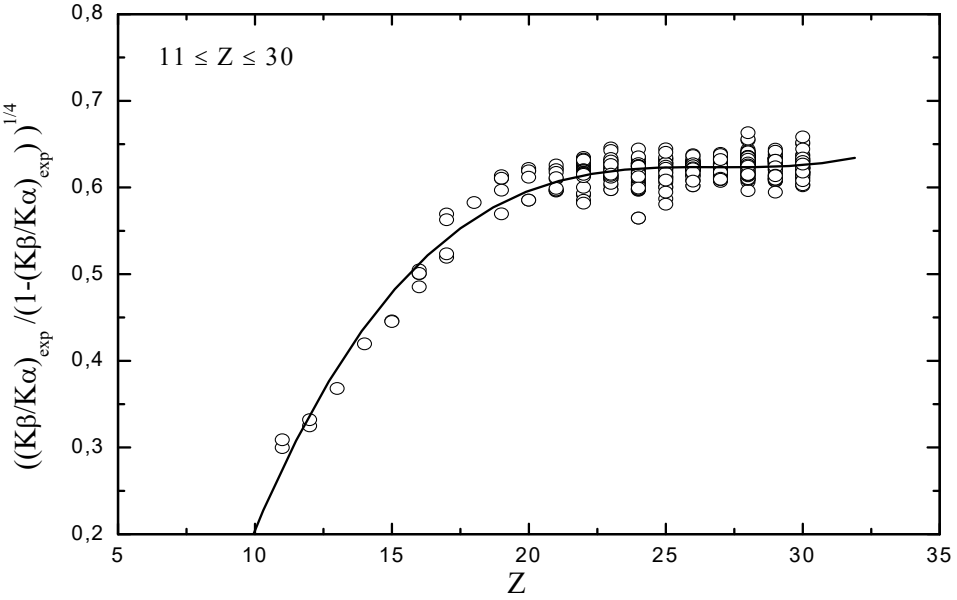

Figure 1: La distribution des valeurs expérimentales réduite des rapports d'intensité: $\left(\frac{(K_\beta/K_\alpha)_{exp}}{1-(K_\beta/K_\alpha)_{exp}}\right)^{1/4}$ pour les éléments11≤Z≤30 en fonction du numéro atomique Z. La courbe de l'interpolation est représenté en trait plein.

Table 1. calcul des rapports d'intensités (K_β/K_α) empirique pour des cibles de 11≤.Z≤30 Les valeurs théoriques, empiriques et expérimentales des autres auteurs sont aussi présentées dans le même tableau.

Z-élément	This Works	Other Works				
		Theo.	Fitt. (empirique)			Exp.
	Emp.	Scofield [4]	Salem et al. [3]	Khan and Karimi [6]	Kahoul et al. [5]	
Z=11, Na	0.0057	-	-	-	-	-
Z=12, Mg	0.0128	-	0.013	0.013	-	-
Z=13, Al	0.0229	0.00611	-	0.014	-	-
Z=14, Si	0.0355	0.01705	0.027	0.025	-	-
Z=15, P	0.0496	0.0309	-	0.042	-	0.0378[a]
Z=16, S	0.0642	0.0467	0.059	0.063	0.0524	0.0609[a]
Z=17, Cl	0.0782	0.0638	-	0.085	0.0693	0.0911[a]
Z=18, Ar	0.0910	0.0818	0.105	0.110	0.0854	-
Z=19, K	0.1021	0.0956	-	0.120	0.0996	0.122[a]
Z=20, Ca	0.1111	0.1065	0.128	0.127	0.1113	0.128[a]
Z=21, Sc	0.1181	0.1106	-	0.131	0.1203	0.129[a]
Z=22, Ti	0.1231	0.1137	0.134	0.131	0.1266	0.132[a]
Z=23, V	0.1265	0.1161	-	0.132	0.1305	0.1479[b]
Z=24, Cr	0.1284	0.1153	0.135	0.133	0.1323	-
Z=25, Mn	0.1292	0.1195	-	0.134	0.1325	0.132[c]
Z=26, Fe	0.1293	0.1208	0.135	0.134	0.1317	0.1342[c]
Z=27, Co	0.1291	0.1218	-	0.135	0.1304	0.137[c]
Z=28, Ni	0.1289	0.1227	0.135	0.136	0.1291	0.138[c]
Z=29, Cu	0.1292	0.1216	-	0.137	0.1283	0.1392[c]
Z=30, Zn	0.1303	0.1241	0.138	0.139	0.1285	0.141[c]

[a]Zararsiz [7]
[b]Chang et al. [8]
[c]Öz [9]

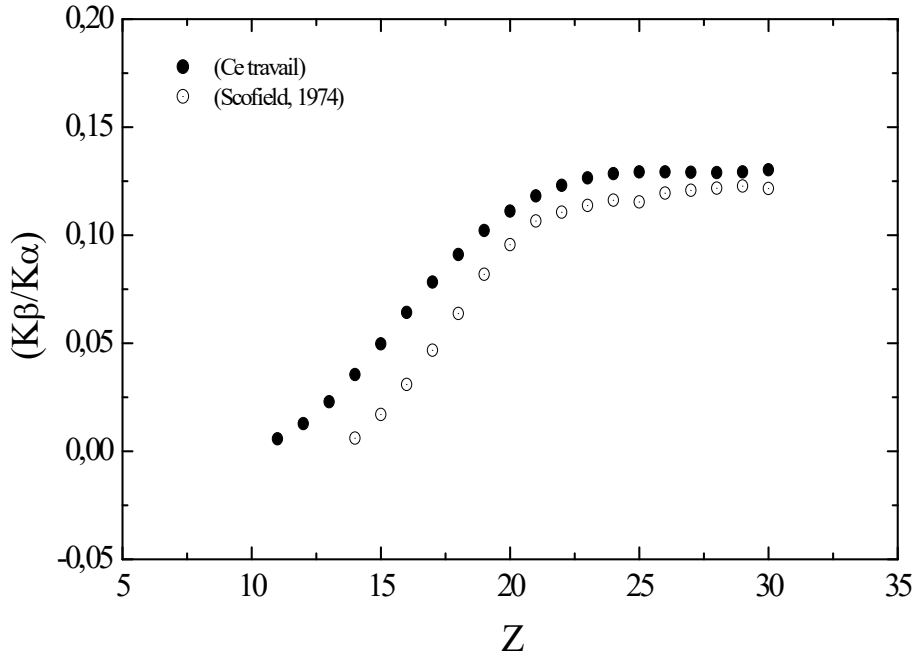

Figure 2 : Nos valeurs empiriques du rapport d'intensité K_β/K_α comparer aux valeurs théoriques de Scofield [4] en fonction du nombre atomique Z.

Dans la figure 3, on observe que les écarts entre nos valeurs empiriques et celles de Salem et al. [3] varies de 1.56 % jusqu'à 23.94% , mais avec les valeurs de Khan et Karimi [6], on a un ecart de 1.56% à 38.86%. Concernant les veleurs de Kahoul et al. [5] la variation de l'écart se trouve entre 0.15% à 18.38%.

Dans la dernière figure (figure 4) on remarque que nos valeurs empiriques du rapport d'intensités sont bien conformes aux valeurs éxpérimentales de Kararsiz [7], Chang et al. [8] and Öz [9]. L'accord varie de 5.14% à 23.79% pour Kararsiz [7], 16.91% pour Chang et al. [8] et de 2.16% à 8.21% pour Öz [9].

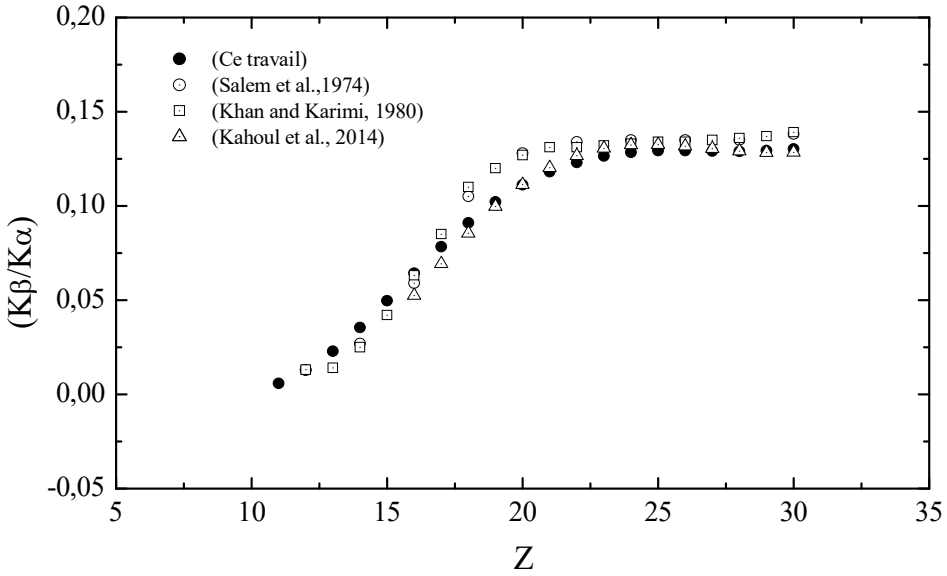

Figure 3 : Valeurs empiriques (présente étude) du rapport d'intensité K_β / K_α comparées aux résultats empiriques de Salam et al. [3], Kahoul et al. [5] et Khan and Karimi [6] en fonction du Z.

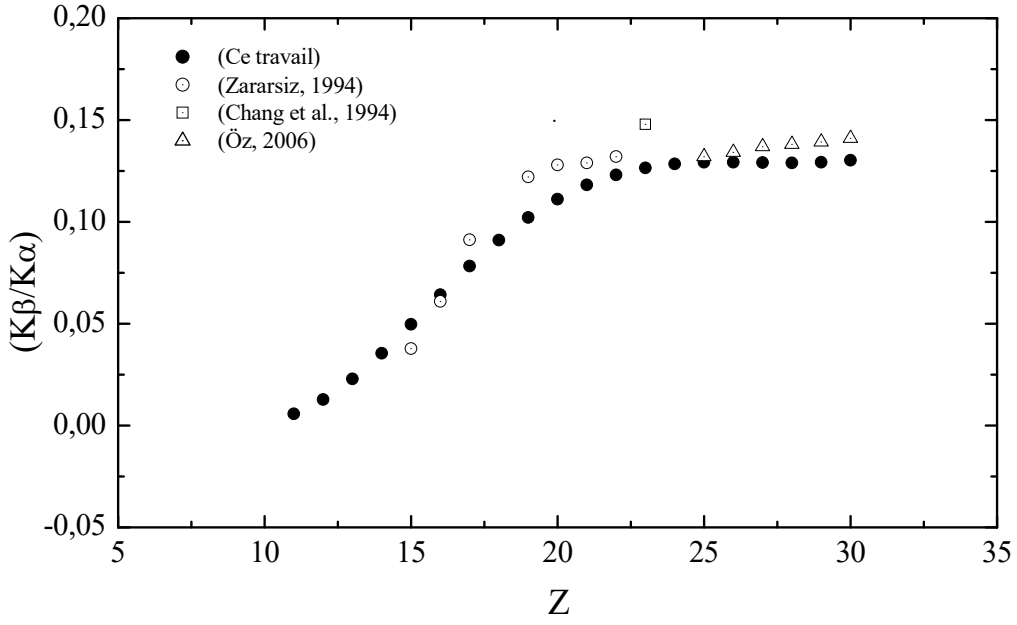

Figure 4 : Valeurs empiriques (présente étude) du rapport d'intensité K_β/K_α comparer aux valeurs expérimentales de Kararsiz [7], Chang et al. [8] and Öz [9] en fonction du nombre atomique Z.

4. Conclusion

Nous avons présenté dans ce travail les résultats du calcul empirique du rapport d'intensité (K_β/K_α) pour les éléments atomique légers excités par des photons. On a calculé le rapport d'intensité (K_β/K_α) pour les elements de $11 \leq Z \leq 30$ à l'aide de la base de données des valeurs expérimentales compilées par différents auteurs. En se basant sur la méthode des moindres carrés, nous avons déterminé une fonction analytiques qui nous a ensuite permis de déduire des valeurs empiriques du rapport d'intensité (K_β/K_α). Les résultats obtenus ont été présentés dans un tableau ainsi qu'une étude comparative à des travaux théoriques, empiriques et expérimentaux d'autres auteurs.

References

[1] S. Daoudi, A. Kahoul, N. Kup Aylikci, J.M. Sampaio, J.P. Marques, V. Aylikci, Y. Sahnoune, Y. Kasri, B. Deghfel. At. Data Nucl. Data Tables 132, 101308 (2020).
[2] G.C. Nelson, B.G. Saunders, S. I. Salem. At. Data Nucl. Data Tables 1, 377-384 (1970)
[3] S. I. Salem, S. L. Panossian, R. A. Krause. At. Data Nucl. Data Tables 14, 91-109 (1974).
[4] J.H. Scofield. Atom. Data Nucl. Data Tables 14, 121-137(1974).
[5] A.Kahoul, N. Kup Aylikci, V. Aylikci, B. Deghfel, Y.Kasri, M. Nekkab. J. Radiat. Res. Appl. Sci. 7, 346-362 (2014).
[6] Md. R. Khan, M. Karimi. X-ray spectrum. 9, 32-35 (1980).
[7] A. Zararsiz. J. Radioanal. Nucl. Chem. 185, 193-197 (1994).
[8] C. N. Chang, C. T. Chen, C. C. Yen, Y. H. Chiou, C. W. Wu, S. K. Su. J. Phys. B At. Mol. Opt. Phys. 27, 5251-5256 (1994).
[9] E. Öz. J. Quant. Spectrosc. Radiat. Transf. 97, 41-50 (2006).

- **Aims and scope:** The Journal of Physical and Chemical Research is an English, French or arabic language peer–reviewed half yearly publication, open access journal, free of charges. The journal edited by: Laboratory of Materials Physics, Radiation and Nanostructures *(*LPMRN), Faculty of Sciences and Technology, Mohamed El Bachir El Ibrahimi University, Bordj-Bou-Arreridj, Algeria. It publishes regular research papers (articles) and short communications. The motivation for this journal is to encourage scientists to publish their experimental and theoretical results in the field of Physical, Chemical and the related subjects. Papers previously published elsewhere cannot be accepted for the journal. Submission must be done at the following email address: jpcr@univ-bba.dz . The acceptance for publication lies on the recommendations of at least two ad hoc referees, and of the editorial board, if necessary.

- **Topics:**
  - Astrophysics and astroparticles
  - Atomic and molecular physics
  - Biological physics
  - Chemical physics and physical chemistry
  - Computational science
  - Condensed matter
  - Fluids and fluid dynamics
  - Gravitation and cosmology
  - Instrumentation and measurement
  - Mathematical physics
  - Medical physics
  - Nuclear physics
  - Optics, quantum optics and lasers
  - Particle physics and field theory
  - Semiconductors
  - Soft matter, liquids and polymers
  - Statistical physics and nonlinear systems
  - Surfaces, interfaces and thin films
  - Thermodynamics
  - Statistical Mechanics and Thermodynamics
  - Molecular Spectroscopy
  - Quantum Chemistry
  - Computational Chemistry
  - Physical Chemistry of Life Sciences
  - Surface Chemistry
  - Catalysis
  - Physical Chemistry of Electrochemistry
  - Kinetics
  - Nanochemistry and Nanophysics
  - Liquid Crystals
  - Ionic Liquid
  - Photochemistry
  - Experimental article of Physical chemistry
  - Mathematical Chemistry

First Legal Deposit: June, 2022